iScience

Article

Multifunctional nanoparticle platform for targeted delivery and vaccines

Graphical abstract

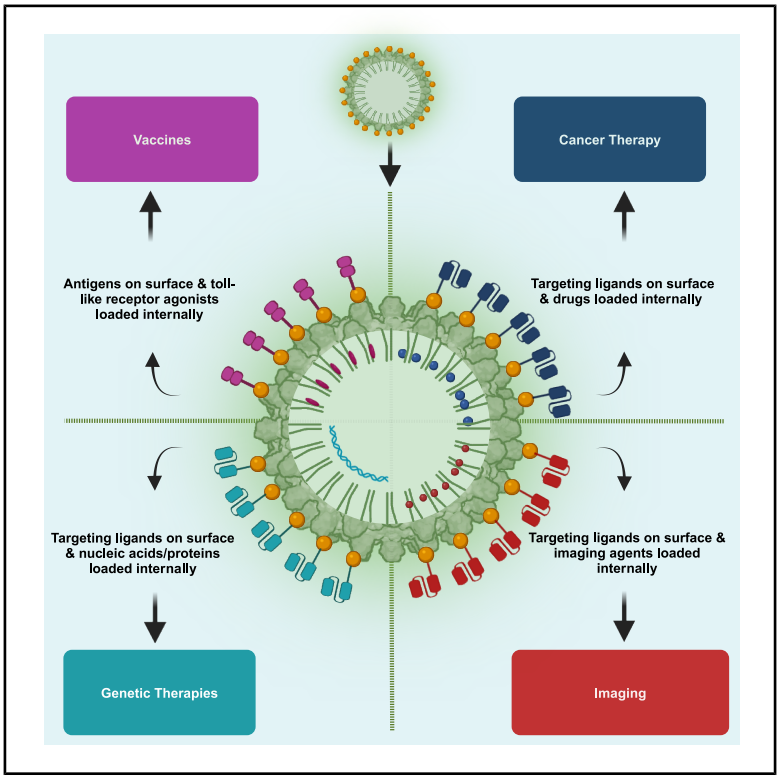

Highlights

- Targeting delivery platform with high yields of versatile virus-like particles
- Reliable production process with in-process and final production testing
- Efficient loading of multiple cargoes with high yield virus-like particle assembly
- Controllable surface modification with multiple adducts using click chemistry

Authors

Anja S. Redecker, Medea Neek, Philip E. J. Smith, James R. Swartz

Correspondence

jswartz@stanford.edu

In brief

Therapeutics; Drug delivery system; Nanoparticles; Biochemistry; Biomaterials

Redecker et al., 2025, iScience *28*, 112599
June 20, 2025
https://doi.org/10.1016/j.isci.2025.112599

CellPress

iScience

CellPress
OPEN ACCESS

Article

Multifunctional nanoparticle platform for targeted delivery and vaccines

Anja S. Redecker,[1] Medea Neek,[1] Philip E.J. Smith,[1] and James R. Swartz[1,2,3,*]
[1]Department of Chemical Engineering, Stanford University, Stanford, CA 94305, USA
[2]Department of Bioengineering, Stanford University, Stanford, CA 94305, USA
[3]Lead contact
*Correspondence: jswartz@stanford.edu
https://doi.org/10.1016/j.isci.2025.112599

SUMMARY

We describe a versatile, targeted delivery platform based on the Hepatitis B core protein virus-like particle (VLP). Multiple protein mutations were combined with cell-free protein synthesis and anaerobic processing to enable reliable production of nanoparticles (NPs) loaded with single or multiple cargoes (typically with concentration factors >10^4) and functionalized with single or multiple surface adducts. Our design supports multiple functional requirements while also enabling flexible and reliable production. Process yields are about 6×10^{13} NPs per mL of cell-free reaction; approximately 100-fold higher than current adeno-associated virus (AAV) yields and 8 times previously reported HBc VLP yields. We demonstrate platform feasibility and versatility by the surface display of a challenging-to-fold dengue fever antigen and by pharmacokinetic studies using whole-body mouse imaging. The platform supports rapid, parallel production of multiple product candidates to increase success rates for targeted therapeutics, gene therapies, imaging agents, and vaccines.

INTRODUCTION

More than a century ago, Nobel Prize winner Paul Ehrlich had a vision: the Magic Bullet.[1] This tiny vehicle would greatly increase medical efficacy while also decreasing side effects by delivering the medicine only to targeted cells. This therapeutic agent would precisely target and eradicate disease-causing cells without harming unaffected, healthy tissue. Here, we report a virus-like particle platform for the rapid development and efficient production of such agents; ''smart'' nanoparticles (NPs) capable of delivering anti-cancer toxins, imaging agents, DNA, and proteins as well as vaccine adjuvants and antigens.

Since pathogenic viruses are highly evolved delivery vehicles, investigators have long sought to exploit viral components for targeted delivery, such as virus-like particles (VLPs)[2–5] which resemble viruses but are non-infectious and replication deficient as they lack viral genetic material. While many different types of VLPs have been studied,[6–8] the adeno-associated virus (AAV) has emerged as one of the most promising candidates, mainly due to its broad tissue tropism and effective, if unreliable, DNA loading. However, several concerns have surfaced which include low cargo capacity, immune responses, difficulties in achieving tissue specificity, and manufacturing challenges.[9] The Hepatitis B core protein (HBc) VLP has become another leading candidate since it is composed of a single, relatively small protein, has a large cavity for cargo loading (ca. 26 nm diameter), and typically offers 120 protruding surface spikes for displaying functional adducts.[10]

For any NP to be a successful product candidate, it must be: (a) well-characterized, (b) economically produced,[11–13] (c) loaded with cargoes,[14–21] and (d) mechanically stable.[22–25] It must also: (e) either evade or stimulate the immune system depending on the application,[26,27] (f) escape from the vasculature,[28,29] (g) be targeted to[30–32] and internalized only by the correct cells, (h) escape from endosomal vesicles,[30] and (i) open to release its cargo in the cytoplasm.[3,33] Figure 1A indicates the design features we have introduced to address these requirements. Here we demonstrate the versatility of this platform by satisfying requirements (a) to (d).

Achieving this versatility has required an unconventional production process (Figure 1B). Leveraging cell-free protein synthesis (CFPS) we introduce non-natural amino acids for later surface functionalization and produce unassembled HBc subunits (monomers and dimers) to facilitate purification and minimize product contamination. Following anaerobic subunit purification and on-column reduction to provide assembly competent HBc subunits, we assemble and load the HBc VLPs in a single procedure. Finally, after VLP stabilization and purification via size-exclusion chromatography (SEC), we surface functionalize the VLPs through the non-natural amino acids.

In developing this process, we found the most common approach for HBc VLP production, *in vivo E.coli* expression,[35–39] to be inadequate since it did not allow access to or control over the protein production environment. In contrast, CFPS[22,40,41] provides such access and control over the expression and folding environment to optimize the production of individual proteins. CFPS utilizes crude cellular extracts capable of

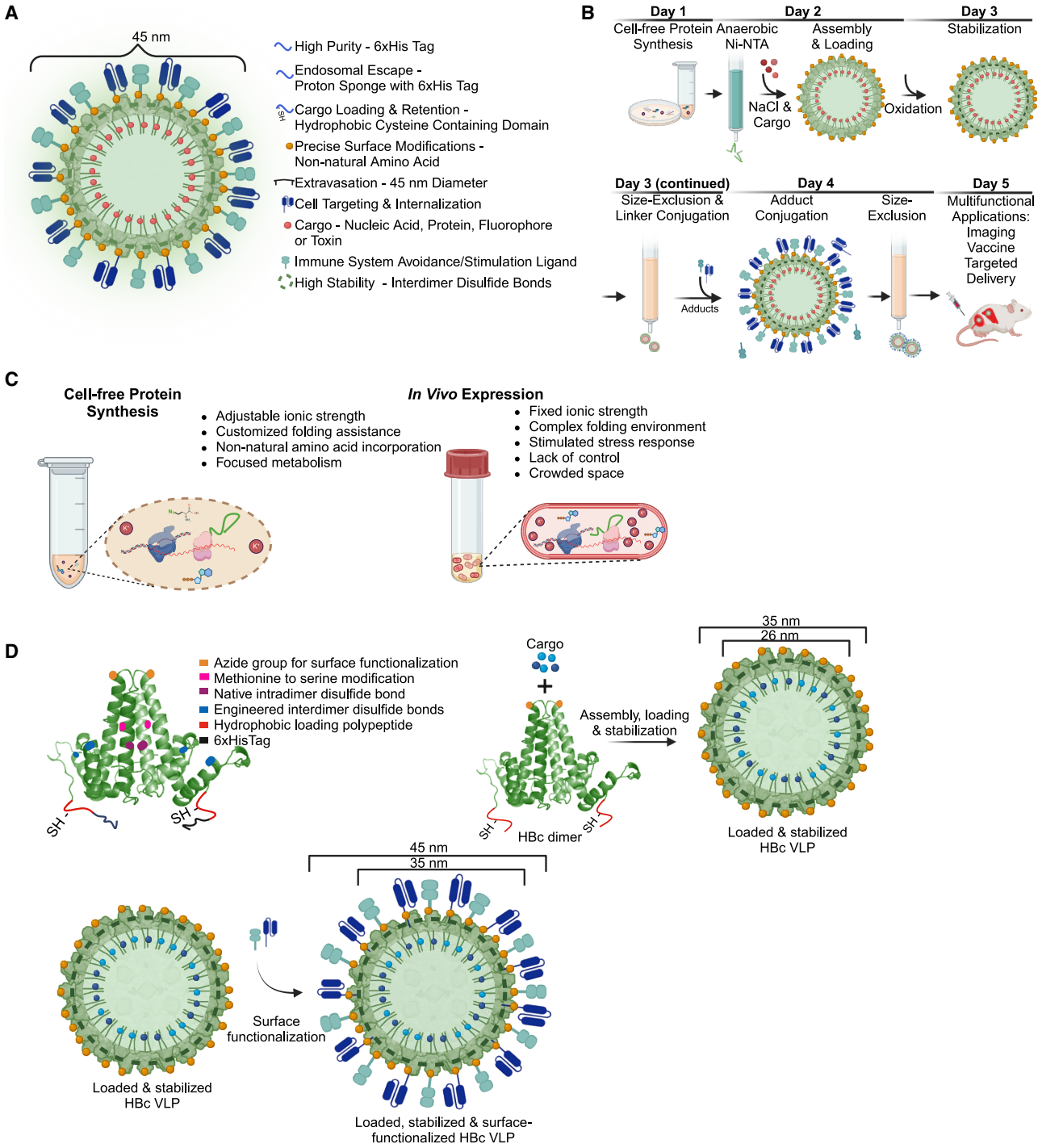

Figure 1. Multifunctional delivery platform, performance requirements, and production overview

(A) Molecular requirements for effective cargo delivery.

(B) Timeline of HBc VLP production process overview.

(C) Comparison of CFPS vs. *in vivo* expression.

(D) HBc dimeric subunit with engineered azide groups (yellow), methionine to serine mutation (pink) (S66M), native intradimer disulfide bond (purple), engineered cysteines for interdimer bonds (blue) (C29 and C107), and a C-terminal extension with a hydrophobic loading domain containing a sulfhydryl group (red) and a polyhistidine tag (black); PDB: 1qgt.[34]

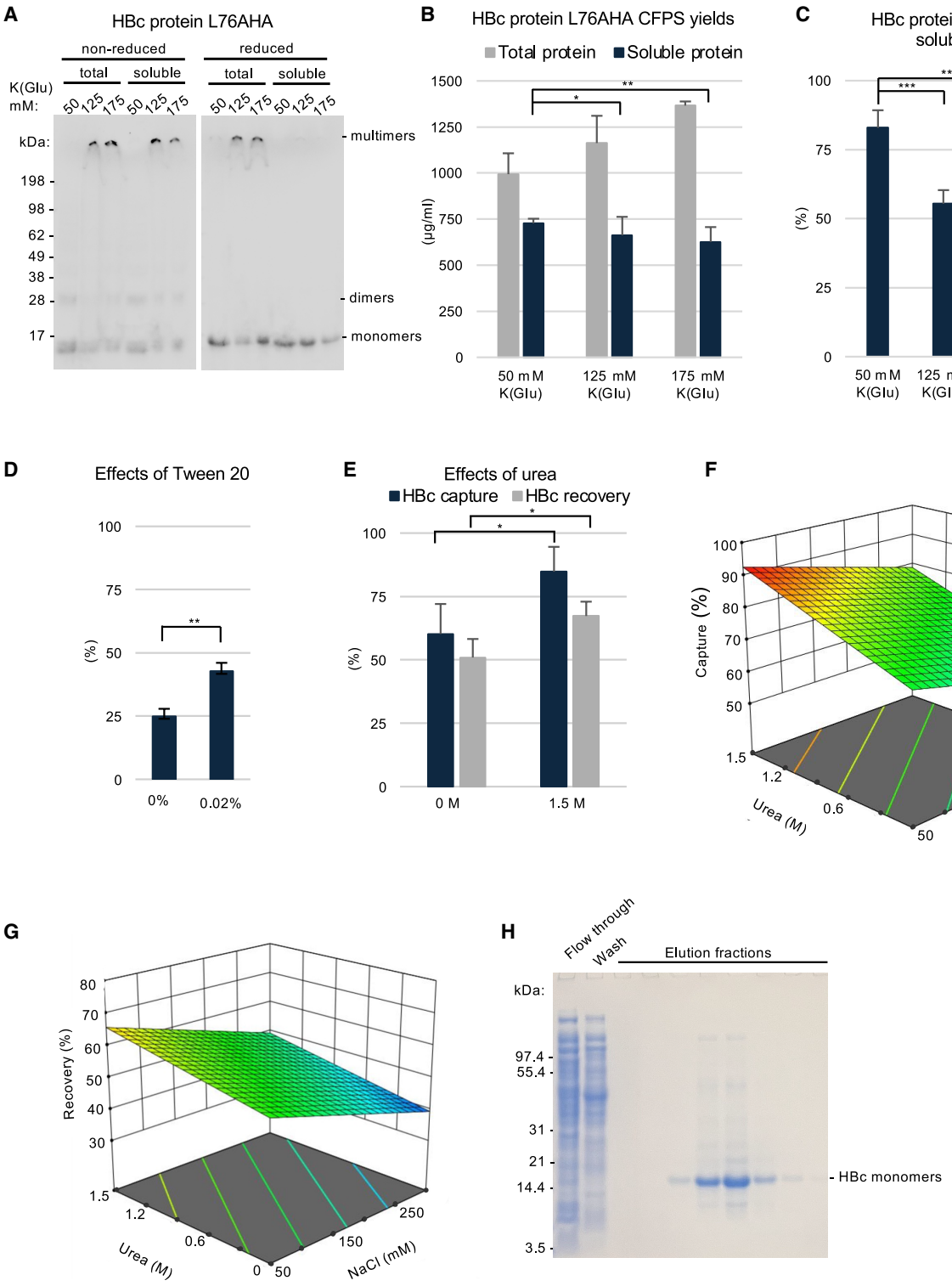

Figure 2. Effects of ionic strength on HBc protein CFPS & Ni-NTA capture and elution

(A) Autoradiograms of HBc proteins produced in CFPS at different KGlu concentrations. Both total and soluble yields are shown in non-reduced and reduced states.

(B) Effects of KGlu concentration on total and soluble yields of HBc protein ($N = 6$) as measured by C^{14} leucine incorporation and scintillation counting ($N = 6$). Error bars indicate standard deviation.

(legend continued on next page)

transcription, translation, and protein folding. The addition of DNA that encodes the protein of interest and a variety of bio-molecules (e.g. cofactors, amino acids, chaperones etc.) activate efficient, cost-effective, and scalable protein production (Figure 1C).[22,42–47] In this study, we demonstrate the benefits of CFPS in a few ways.

First, we express VLP subunits at lower ionic strengths to avoid triggering VLP assembly.[22,48] The VLP subunits can then be purified via Ni-NTA chromatography to fully remove contaminants that would otherwise be trapped inside the assembled VLPs. Furthermore, it eliminates additional, time-consuming and often harsh disassembly-assembly steps for VLP purification and cargo loading that are commonly performed with *in vivo* VLP production systems.[36,49,50] This also enables efficient Ni-NTA purification without harsh denaturing conditions, which have previously been necessary.[38,51]

Second, we incorporate non-natural amino acids for site-specific conjugation of adducts to functionalize the particle's surface. Site-specific surface functionalization via click conjugation circumvents limitations of unspecific conjugation via NHS ester chemistry, interference with protein folding through polypeptide insertions, and possibly added immunogenicity associated with the SpyCatcher system.[3,52] To accomplish this, we mutate the HBc protein (Figure 1D) by both changing a native methionine to serine so that azidohomoalanines (AHAs) can be incorporated using methionine replacement, and by mutating either codon 76 or 80 with ATG to incorporate two AHA's at the tip of each dimeric spike.

Next, after Ni-NTA purification, we improve cargo loading by adding a hydrophobic C-terminal loading domain with a cysteine residue (IGIGIC) (Figure 1D) to attract cargo during VLP assembly and retain it through reversible disulfide bond formation or irreversible maleimide conjugation. We achieve versatile loading of diverse molecules: a cancer toxin, fluorophores, DNA, and a protein. By using maleimide conjugation, we accomplish loading efficiencies of 86% for super-folder green fluorescent protein, 87% for a fluorophore, and 95% for a single-stranded DNA. This results in major cargo condensation during loading with the internal concentration of the cargo approximately 10^4 higher than that in the surrounding reaction solution. Furthermore, we demonstrate simultaneous loading of two different cargoes which to our knowledge has not been done before with the HBc VLP.

In addition to internal loading, we also demonstrate efficient external surface functionalization using the non-natural amino acids previously incorporated during CFPS. This is facilitated by bifunctional linkers, using strain-promoted azide-alkyne cycloaddition (SPAAC) or maleimide conjugation in combination with an inverse-electron-demand Diels-Alder reaction (IEDDA). We demonstrate attachment of polyethylene glycol (PEG) and a Dengue fever vaccine antigen, obtaining VLP spike surface modification of 100% and 95% respectively. Additionally, we show attachment of a fluorophore as well as simultaneous, efficient, and controllable ratios of co-attached PEG and the vaccine antigen.

Importantly, we show that our VLPs—leveraging previously reported improvements on VLP stabilization using a disulfide bond network[22]—are stable for 3 months at 4°C. This is a beneficial advantage as it can accelerate process development by facilitating the production and testing of multiple drug candidates sequentially or in parallel. Additionally, inconvenient cold chain requirements can be avoided for vaccines derived from the stabilized HBc VLP. Finally, we use whole-body imaging to demonstrate how fluorophore loading and PEG surface additions can facilitate pharmacokinetic studies.

RESULTS

Avoiding premature assembly during CFPS

To produce high quality, precisely loaded, and surface-modified NPs it was critical to first purify the VLP subunits. Ni-NTA affinity chromatography offered specificity, but premature VLP assembly prevented adequate subunit capture.

CFPS, in comparison to *in vivo* expression, offered direct control over the synthesis and folding environment. As potassium and glutamate (KGlu) are the dominant ions in the *E. coli* cytoplasm,[53,54] CFPS is typically conducted at around 175 mM KGlu.[55] However, since higher ionic strengths trigger VLP assembly, we evaluated lower KGlu concentrations (50 and 125 mM). SDS-PAGE analysis (Figures 2A and S1A) confirmed subunit aggregation, and premature VLP assembly was largely avoided with 50 mM KGlu. Although total yields decreased, soluble yields increased to about 750 μg/mL (Figures 2B, 2C, and S1B). Later experiments showed that increasing the amount of cell extract in the CFPS reaction from 25% to 35% increased soluble yields to ca. 1 mg/mL (Figure S1B), easily detectable by SDS-PAGE (Figure S1C). Such adjustments are not possible with *in vivo* production.

Improving Ni-NTA capture and elution

Even with premature assembly avoidance, early Ni-NTA based purifications yielded only 25% recovery (Figure 2D). Adding two additional histidines (8xHis-tag) was not helpful for purification and decreased CFPS soluble yields by about 40% (Figure S1D). Hypothesizing that the C-terminal hydrophobic loading domains might be self-associating and hiding the 6xHis-tags, we added 0.02% polysorbate 20 (Tween 20) to the buffer exchange post-CFPS and the recovery efficiency increased to ca. 45% (Figure 2D).

Since previous reports suggested that chaotropic agents could improve Ni(NTA) capture,[38,51] we next conducted a design of experiments survey analyzing the effects of urea and NaCl

(C) HBc protein solubility (%) as a function of CFPS KGlu concentration. Error bars indicate standard deviation ($N = 6$).
(D) Tween 20 effect on HBc recovery. Error bars indicate standard deviation ($N = 3$).
(E) Differences in capture and recovery of HBc proteins using urea. Error bars indicate standard deviation ($N = 3$).
(F) 3D graph of HBc capture efficiency (%) versus urea and NaCl concentrations.
(G) 3D graph of HBc elution efficiency (%) versus urea and NaCl concentrations.
(H) Non-reducing SDS-PAGE after Ni-NTA purification. Significance: $^*p \leq 0.05$; $^{**}p \leq 0.01$; $^{***}p \leq 0.001$; $^{****}p \leq 0.0001$. See also Figure S1.

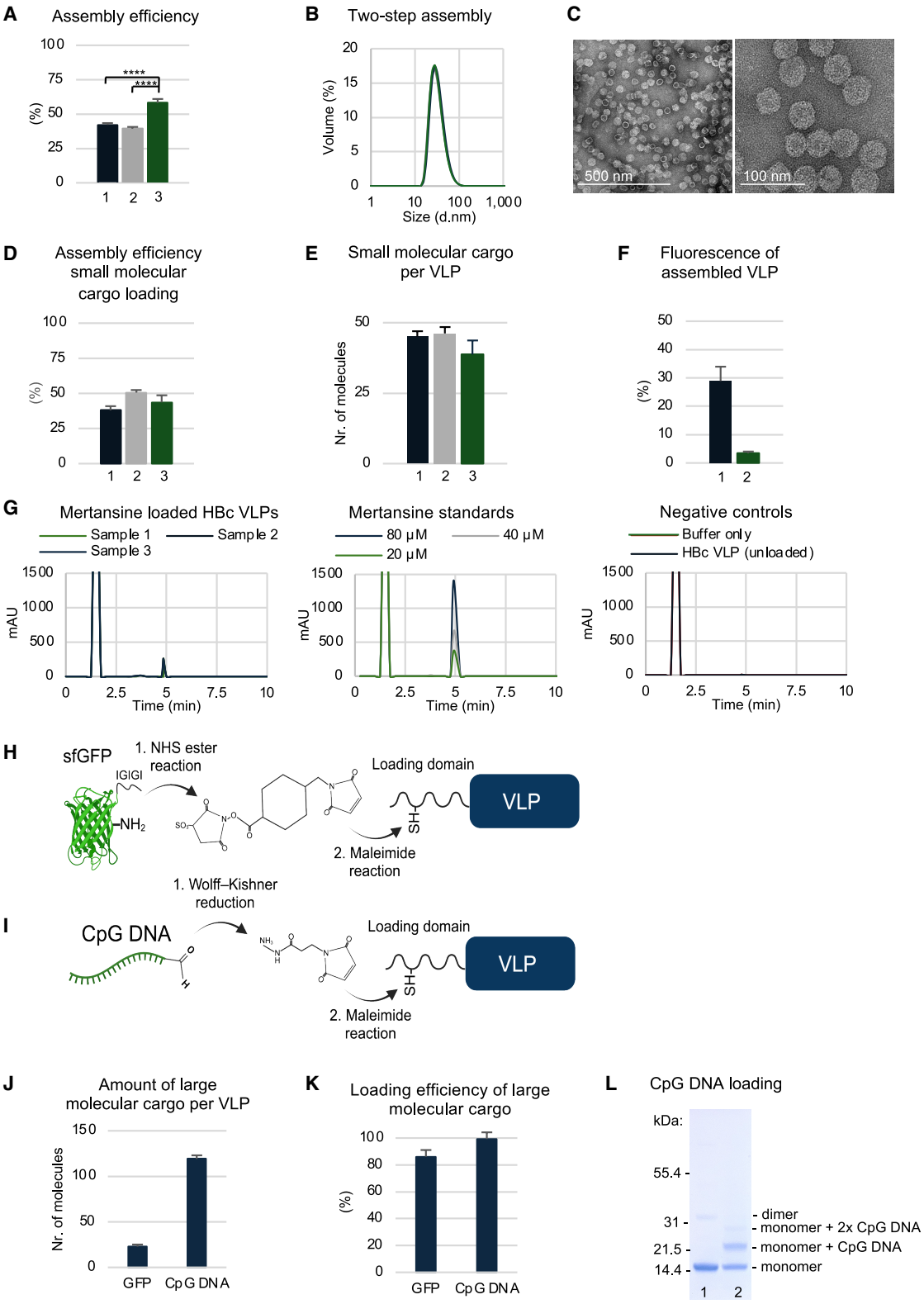

Figure 3. VLP assembly quantification, quality assessment, and loading

(A) VLP assembly efficiencies using: (1) one-step NaCl to HBc addition, (2) one-step HBc to NaCl addition and (3) two-step NaCl addition. Error bars indicate standard deviation (*N* = 3).

(legend continued on next page)

(Figures 2E–2G). The addition of 1.5 M urea to the post-CFPS buffer exchange raised binding efficiency to ca. 85%, most likely by further increasing 6xHis-tag accessibility. Although 3 M urea further improved recovery, VLP assembly then dramatically decreased suggesting persistent HBc structural damage. Contrary to the Ni(NTA) resin supplier's guidance, decreasing the NaCl concentration improved recovery, most likely by avoiding HBc subunit aggregation. The adopted changes improved product recovery by 3.5-fold while also providing a relatively pure HBc product (> 95%) (Figure 2H).

Optimization of VLP assembly

The assembled T = 4 HBc VLPs (ca. 35 nm outer diameter) consist of 120 dimers, each potentially stabilized by a native intradimer disulfide bond.[56] As mentioned, capsid assembly can be triggered by NaCl addition. Initially however, VLP assembly was ineffective with insoluble aggregates dominating after NaCl addition. We confirmed a report by Selzer et al.[57] indicating assembly inhibition by preformed intradimer disulfide bonds. After additionally including 1 mM dithiothreitol (DTT) in all solutions from CFPS to VLP assembly, the assembly efficiency increased to 42% (Figure 3A).

However, subsequent azide-alkyne click reactions for VLP surface modification were then unsuccessful. A report by Handlon and Oppenheimer had shown rapid DTT-mediated reduction of azidothymidine to aminothymidine.[58] Since their reported rate constants predicted minimal azide loss with a 15-min, 5 mM DTT exposure; the subunits were briefly reduced while bound to the Ni(NTA) column. Additional experimentation indicated that this exposure provided effective VLP assembly and VLP quality was confirmed by dynamic light scattering. To avoid reformation of the problematic disulfides by oxygen-mediated oxidation before assembly, all purification and assembly steps were thereafter performed anaerobically.

In efforts to further improve assembly efficiency, we found that adding VLP subunits to the 1 M NaCl solution vs. salt to subunits was not beneficial (Figure 3A); nor were changing NaCl concentration and/or addition rate. As previous studies have shown that HBc VLP assembly proceeds via partially assembled intermediates and that assembly rate increases with higher ionic strength,[48,59–61] we decided to slowly increase the NaCl concentration to 0.3 M NaCl and add a short incubation period of 10 min before proceeding to increase it to the final concentration of 1M. Using this two-step approach, the assembly efficiency increased from about 40% to nearly 60% (Figure 3A). For VLP stabilization, both intra- and interdimer disulfides were then formed by a 30-min incubation with 500 μM H_2O_2. Correct VLP formation after SEC purification was confirmed by DLS analysis and transmission electron microscopy (TEM) which shows both T = 3 (ca. 30 nm diameter) and T = 4 (ca. 35 nm diameter) HBc VLPs. (Figures 3B and 3C). DLS analysis after 3 months of storage at either −80°C or 4°C detected no deterioration in VLP quality (Figures S2C–S2E).

Loading molecular cargoes

With an inner diameter of about 26 nm, the hollow HBc VLP offers a cargo volume about three times larger than that of AAV particles[62–64] and is therefore suitable for delivering micro- and macromolecular loads. However, to accomplish efficient cargo loading, cargo condensation by a factor of about 10^4 is required as the cargo volume after assembly is only 0.05% of the volume of the surrounding solution. Additionally, it is essential that the cargo does not interfere with VLP assembly by distorting subunit structures or inhibiting correctly orientated dimer-to-dimer interactions. Despite these challenges, we demonstrate the versatility of our two-step, combined loading and assembly procedure by loading a fluorophore as an imaging agent, an anti-tumor toxin, the Toll-like receptor (TLR) agonist CpG DNA as a vaccine adjuvant, and superfolder green fluorescent protein (sfGFP).

Early work by us and others[65] showed that smaller molecular weight cargoes such as fluorophores and cancer toxins can be lost by diffusion through multiple pores in the VLP shell (diameters ≈17–20 Å). These cargoes therefore require covalent tethering to the VLP's inner surface; either by persistent maleimide bonds for cargoes such as fluorophores, or by conditionally stable bonds such as disulfides which can be reduced in the target cell's cytoplasm to release the agent.[22] Among several candidates, we identified an IGIGIC hydrophobic loading domain as an HBc C-terminal extension with good cargo adsorption, minimal VLP assembly interference, and a reactive cysteine for tethering.

To demonstrate effective and versatile cargo loading, we loaded (a) Alexa Fluor 750 maleimide (AF750M), (b) an aldehyde modified CpG DNA fused to a maleimide hydrazine linker, (c) a

(B) DLS analysis of assembled VLPs with mean diameter = 33 nm.
(C) TEM of VLPs.
(D) VLP assembly efficiency after loading of small molecules using: (1) one-step procedure for AF750M, (2) two-step for AF750M and (3) two-step for dual AF750M and mertansine loading. Error bars indicate standard deviation (N = 3).
(E) Number of small molecules loaded per VLP using: (1) one-step procedure for AF750M, (2) two-step for AF750M and (3) two-step for dual AF750M and mertansine loading (showing mertansine load, AF750M loading was unchanged). Error bars indicate standard deviation (N = 3).
(F) Fluorescence of assembled AF750M loaded VLPs in comparison to disassembled VLPs with (1) 0.22:1 and (2) 1:1 AF750M to HBc monomer molar addition ratios. Error bars indicate standard deviation (N = 3).
(G) HPLC analysis of mertansine cargo after being co-loaded with AF750M during VLP assembly (N = 3).
(H) Loading mechanism for sfGFP starting with NHS ester reaction of the linker to the sfGFP followed by attraction of the protein by the hydrophobic extension and a maleimide conjugation of the sfGFP-linker to the cysteine residue within the VLP's loading domain.
(I) Loading mechanism of CpG DNA starting with a Wolff-Kishner reduction of the linker to the CpG DNA's 5′ aldehyde group followed by maleimide conjugation of the assembled CpG DNA-linker fusion to the VLP's loading domain.
(J) Amount of large molecular cargoes loaded using two-step assembly (N = 3). Error bars indicate standard deviation.
(K) Loading efficiency of large molecular cargo using two-step procedure (N = 3). Error bars indicate standard deviation.
(L) Reduced SDS-PAGE of (1) unloaded VLPs as a control and (2) CpG DNA loaded VLPs. Significance: ****$p \leq 0.0001$. See also Figure S2.

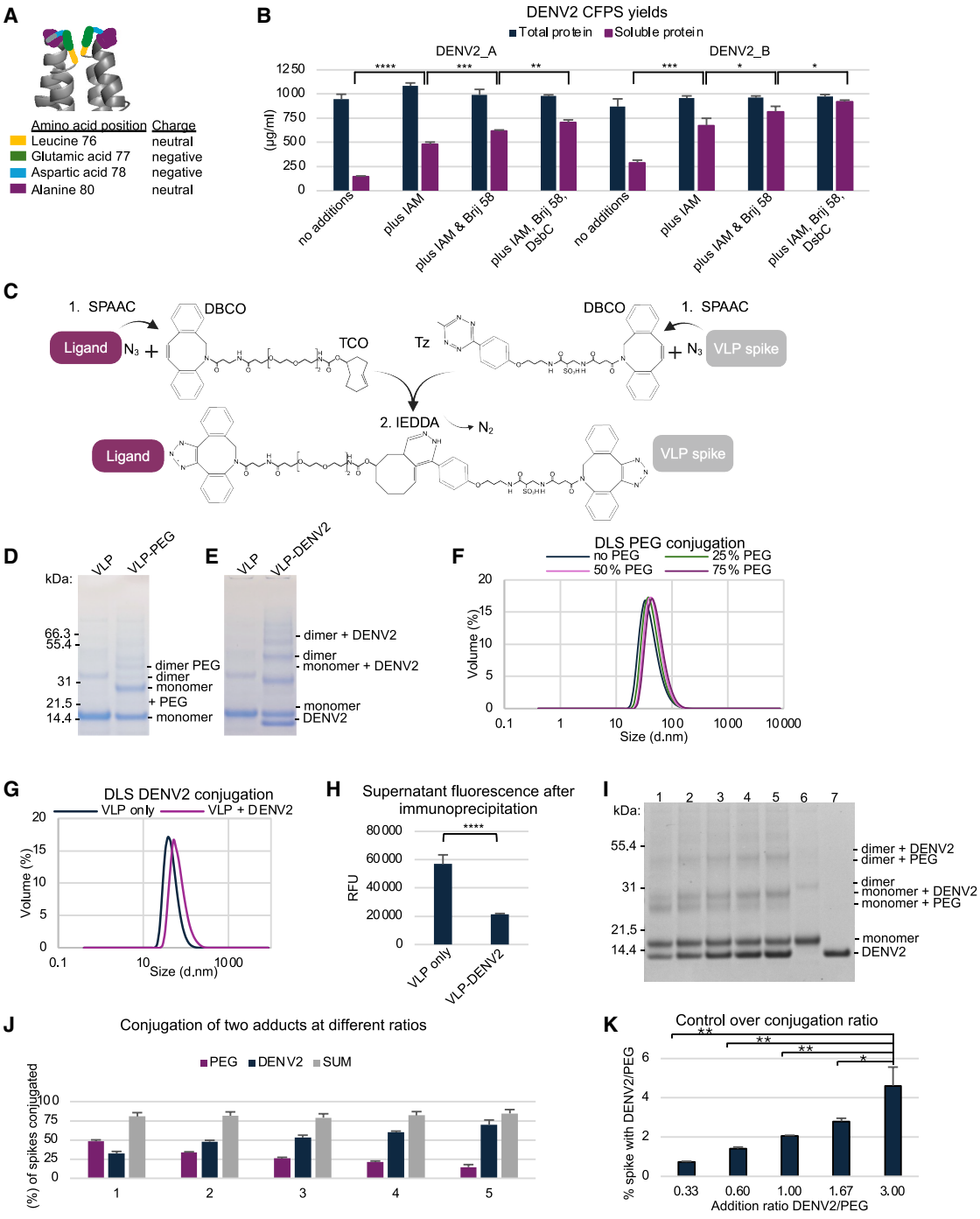

Figure 4. VLP surface functionalization

(A) HBc dimeric subunit spike tip with possible conjugation sites and their respective charges (PDB: 1qgt).[34]

(B) Effects of IAM, Brij 58 and DsbC on the total and soluble protein yields of DENV2 antigen domains with a cysteine residue incorporated for conjugation close to the (A) N- or (B) C- terminus. Yields were measure by C^{14} leucine incorporation and scintillation counting ($N = 3$). Error bars indicate standard deviation.

(C) Surface functionalization of HBc VLPs with (1) attachment of linker via strain-promoted azide-alkyne cycloaddition (SPAAC) to the ligand and VLP's spike followed by (2) inverse-electron-demand Diels-Alder reaction between the ligand's and the VLP's linker.

(D) Reduced SDS-PAGE of VLP conjugated with mPEG-azide (5000) via TCO DBCO linker with molar ratios of HBc monomer to mPEG-azide of 1:1.

(E) Reduced SDS-PAGE of VLP conjugated with DENV2 via a TCO maleimide linker with a molar ratio of HBc monomer to DENV2 of 1:1.5.

(F) DLS of VLPs conjugated with increasing amounts of PEG (5000) per VLP spike (% of that required to modify all spikes). Unconjugated PEG was removed via SEC.

(legend continued on next page)

superfolder green fluorescent protein (sfGFP) attached to an NHS ester maleimide linker (the maleimide moieties can rapidly and irreversibly bind to the loading domain cysteine), and (d) an anti-cancer toxin, mertansine (DM1), with an exposed sulfhydryl.

Beginning with AF750M loading for mouse whole-body imaging, we tested three loading approaches: (1) diffusion into the VLP after stabilization, (2) loading during one-step assembly with the cargo added directly after the salt addition, and (3) loading during the two-step assembly with cargo addition after the initial 10-min incubation at the lower NaCl concentration. The first method was not effective, but both approaches 2 and 3 loaded about 85% of the cargo while VLP assembly was increased from 38% to 50% using the two-step assembly (Figures 3D and 3E). In a classic case of "less is more", loading about 200 dye molecules per VLP resulted in such severe self-quenching (Figure 3F) that the VLPs could not be detected after i.v. injection in the mice. Self-quenching is a phenomenon where the fluorescence intensity of a fluorophore decreases due to the proximity of multiple fluorophores, resulting in interactions that reduce their ability to emit light.[66] In contrast, loading only about 53 molecules per VLP increased the fluorescence approximately 10-fold and provided high quality whole-body mouse images (as shown in the pharmacokinetic study below).

We next sought to load two different cargoes into the same VLP, AF750M, and the anti-cancer toxin (DM1), to offer both tumor imaging and cancer treatment with the same VLP. The hydrophobic toxin DM1 was added 2 min after the AF750M addition at a ratio of 2.5 DM1 molecules per HBc monomer. The sequential addition was performed to prevent AF750M and DM1 from binding to one another and not to the loading domain. As the maleimide reaction is quick and irreversible, AF750M was added first and allowed to react with the loading domain before adding DM1. High-performance liquid chromatography (HPLC) analysis (Figure 3G) indicated the loading of about 40 DM1 molecules per VLP resulting in a loading efficiency of nearly 7%. AF750M loading was not affected and DLS analysis indicated absence of aggregates and multimers after SEC (Figure S3F).

The macromolecules, CpG DNA with a 5′-aldehyde addition and sfGFP with a hydrophobic IGIGIG C-terminal extension were loaded by first attaching the indicated linker to the macromolecule (Figures 3H and 3I) and then adding the linker-modified CpG DNA or sfGFP to the assembly reaction after the first salt addition and a short incubation time. Approximately 114 DNA and 23 sfGFP molecules per VLP were loaded (Figures 3J–3L) with loading efficiencies of 95% and 86%, respectively. VLP assembly and quality was verified by DLS analysis (Figures S2G and S2H). Table 1 shows the estimated cargo loading efficiency and condensation factors. Our two-step combined loading and assembly approach provides efficient loading by typically encouraging very high condensation factors. The exception is DM1 loading most likely both due to occupancy of loading domains by previously loaded AF750M and because the disulfide bond stabilization was delayed relative to the maleimide conjugation.

Versatile modification of the VLP surface through click conjugation

Our next challenge was to site-specifically surface functionalize the VLPs. Using cell-free technology, non-natural amino acids can be conveniently incorporated. Here, we used methionine replacement to introduce azido-homoalanine (AHA) at the VLP's spike tips. This enables site-specific azide-alkyne click conjugation of ligands to the VLP's outer surface.

To demonstrate feasibility for versatile NP surface modification we attached three different ligands to the VLP's surface: (1) PEG, (2) a vaccine antigen, and (3) a fluorescent dye. Figure 4A shows the amino acids displayed on the VLP spike tips. As previously reported,[22] replacing the negatively charged residues dramatically hindered VLP assembly. Initially, Cu(I)-mediated click reactions were evaluated. Incorporating AHA at position 80 versus position 76 for azide display supported better surface conjugation, but SDS-PAGE gel analysis suggested protein damage and low, variable attachment efficiency (Figure S3A). To avoid the use of Cu(I) in attaching PEG to the VLP surface, a sulfo-dibenzocyclooctyne (DBCO) maleimide linker (DBCOM) was first attached to the adduct molecule 6 kDa methoxy-PEG-thiol (mPEG thiol). This fusion was then conjugated to the VLP (Figure S3B). SDS-PAGE densitometry analysis suggested that mPEG thiol was conjugated to approximately 72% of the VLP spike tips.

Next, we expressed domain 3 of surface protein E from the Dengue fever virus 2 as a potential vaccine antigen.[67] A new cysteine was incorporated in either the N-terminal (DENV2 A) or the C-terminal region (DENV2 B) so that VLP surface attachment would display the neutralizing antigen as the outermost surface feature. Again, CFPS offered critical versatility for antigen production providing control over the SH/S-S redox potential for efficient internal disulfide bond formation as well as convenient addition of non-natural agents to improve product folding and solubility. To further encourage correct disulfide bond formation, the *E.coli* S-S bond reductases were inactivated by pretreating the CFPS cell extract with iodoacetamide (IAM). Addition of the *E.coli* disulfide bond isomerase DsbC[43] and the surfactant Brij 58 further improved folding and solubility (Figure 4B). DENV2 B was used as it provided higher soluble product yields. Ni(NTA) purification and attachment of the DBCOM linker then enabled conjugation to the VLP as evidenced by PAGE gel analysis (Figure S3B). Densitometry analysis suggests that DENV2 B was conjugated to ca. 30% of the VLP spike tips.

(G) DLS of VLPs before and after conjugation with DENV2.
(H) Fluorescence of supernatant after immunoprecipitation of VLP and VLP-DENV2 with an anti-DENV2 antibody ($N = 3$). Error bars indicate standard deviation.
(I) Reduced SDS-PAGE and (J) densitometry analysis of simultaneous DENV2 and PEG conjugation after reactions with varying numbers of adducts per HBc monomer: (1) 0.25 and 0.75, (2) 0.375 and 0.625, (3) 0.5 and 0.5, (4) 0.625 and 0.375, and (5) 0.75 and 0.25 of DENV2 and PEG, respectively ($n = 3$). HBc monomer (6) and DENV2 (7) were controls ($N = 3$). Error bars indicate standard deviation.
(K) Analysis of ratio of DENV2 over PEG surface functionalized spikes (%) in relation to addition ratio of DENV2 over PEG ($N = 3$). Error bars indicate standard deviation. Significance: $^{*}p \leq 0.05$; $^{**}p \leq 0.01$; $^{***}p \leq 0.001$; $^{****}p \leq 0.0001$. See also Figure S3.

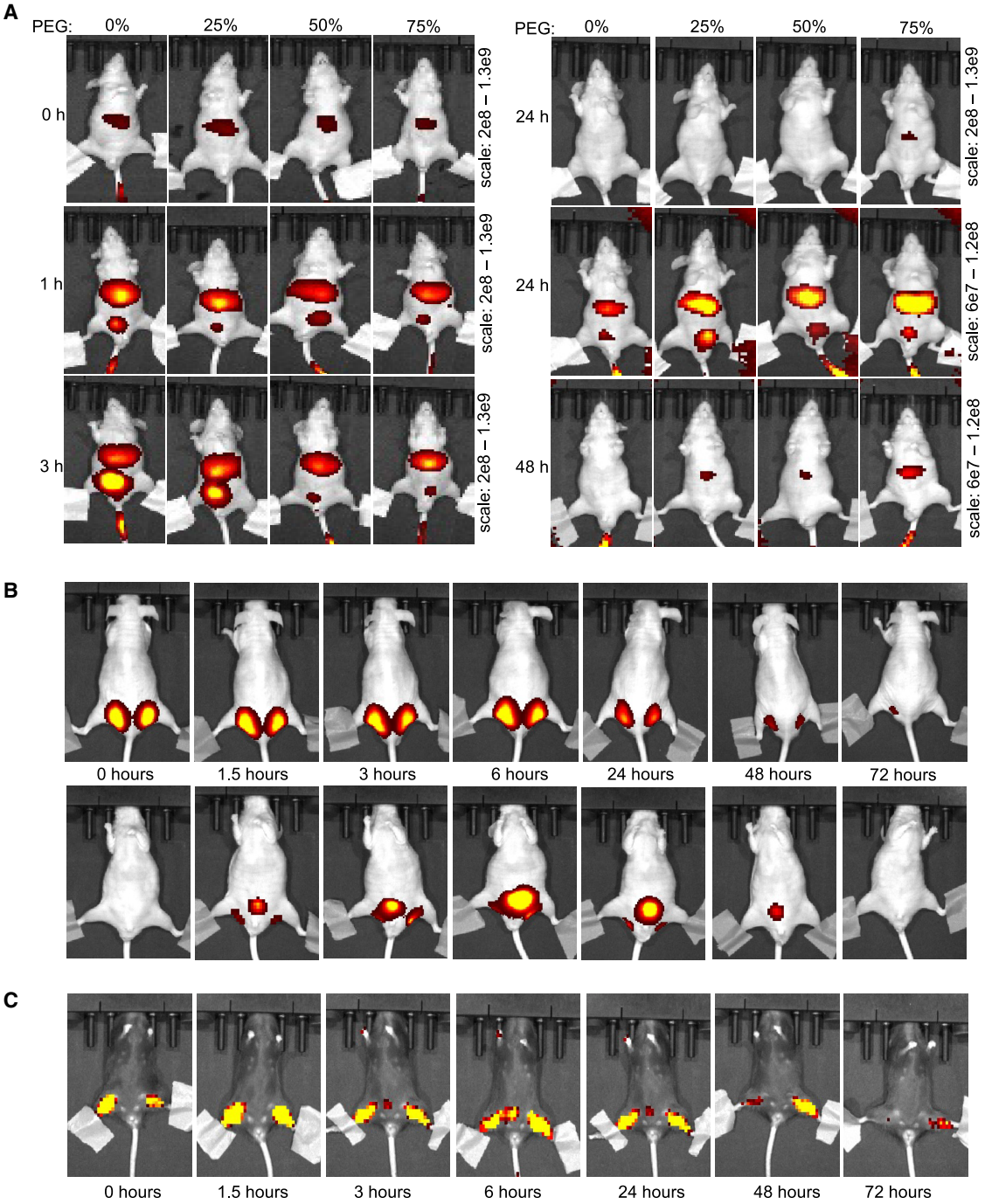

Figure 5. Mouse imaging after injection with AF750M loaded VLPs

(A) 75 μg doses of VLPs with different degrees of PEG conjugation (% of spike tips covered) were injected into the lateral tail vein of nude mice; ventral view. Color scale is set to yellow being maximum and dark red minimum fluorescence. The 24 h time point is shown at two different intensities to allow comparison with earlier assessments.

(B) Mouse imaging after bilateral s.c. 100 μg AF750M VLP injections on the dorsal surfaces near the tail, (top) dorsal views with the color scale set to $5e^9$ (yellow) maximum, and $8e^8$ (dark red) minimum and (bottom) ventral views with the color scale set to $9.5e^8$ (yellow) maximum, and $2e^8$ (dark red) minimum.

(C) Ventral images after bilateral i.m. 100 μg injections into black mice. The color scale was set to $1.45e^8$ (yellow) maximum, and $8.1e^7$ (dark red) minimum. See also Figure S4.

Table 1. Summarizing loading efficiency and achieved condensation factors after two-step loading

Cargo	Loading efficiency (%)	Condensation factor
Single load		
AF750M	85%	14,000
sfGFP	86%	16,000
CpG	95%	47,000
Dual load		
AF750M	85%	14,000
DM1	6.67%	176

To improve conjugation efficiency, we tested the inverse-electron demand Diels-Alder (IEDDA) reaction[68] (Figure 4C). We attached a tetrazine DBCO linker to the VLP's spike tips, a *trans*-cyclooctene (TCO) DBCO linker to mPEG-azide and a TCO-maleimide linker to DENV2. Densitometry analysis of SDS-PAGE suggests 100% coverage of VLP spike tips by PEG (Figure 4D) and 95% coverage by DENV2 (Figure 4E). DLS analysis confirmed increased size of the conjugated VLPs (Figures 4F and 4G). To verify correct antigen display by the AF750M loaded VLPs, an immunoprecipitation with an anti-DENV2 antibody bound to protein G beads was performed and the fluorescence in the supernatant was measured (Figure 4H). The fluorescence dropped significantly for the VLPs conjugated with DENV2B ($p < 0.001$) indicating that the antigen had retained its correct conformation and was effectively displayed. The incomplete immunoprecipitation is possibly caused by the inability of the decorated VLPs to enter the pores of the Sepharose beads due their size. Next, we tested the ability to control the ratio of attached adducts by simultaneous conjugation of PEG and DENV2B with varying the ratios of the two ligands. SDS-PAGE analysis showed changing intensities of the conjugation bands relative to how many ligands were added to the conjugation reactions with consistent coverage of approximately 80% of the spike tips (Figures 4I–4K).

Additionally, we also demonstrated attachment of sulfocyanine7 DBCO, a near infrared fluorophore, to the VLP's outer surface for whole-body imaging when using VLPs loaded with two different therapeutic cargoes.

Initial pharmacokinetic study using VLPs loaded with AF750M

To assess tissue targeting and retention as well as route and rate of elimination, we injected AF750M loaded VLPs subcutaneously (s.c.), intramuscularly (i.m.), and intravenously (i.v.) into either nude athymic or black domestic mice. Figure 5A shows representative whole-body images after injecting AF750M loaded VLPs with increasing amounts of PEG conjugated to the spike tips. Increased PEG coverage of the VLPs' surface decreased the rates of liver uptake and fluorophore elimination via the kidneys into the urine. The pharmacokinetic persistence was increased by more complete PEG coverage. After 72 h, minimal fluorescence was detectable in the mice injected with PEG decorated VLPs (Figure S4A). As expected, the AF750M loaded VLPs with unmodified surfaces persist longer after s.c. and i.m. administration compared to i.v. injection, again with eventual fluorophore elimination in the urine (Figures 5B, 5C, and S4B–S4D). Importantly, organ evaluation after sacrifice of the i.m. injected mice indicated fluorophore deposition in the central iliac lymph nodes that collect lymphatic drainage from the injection sites (S4E).[69] Even though surface fur attenuated the fluorescence signal in the black mice, local NP retention and elimination could still be followed. Such imaging will be highly beneficial for developing targeted therapeutic delivery vehicles as well as vaccines as evidenced by previous reports.[70,71]

As a final note, throughout the course of this study, we produced 28 batches of VLPs with and without different cargos and with and without various surface functionalization. All of the production lots were successfully completed with similar final yields.

DISCUSSION

In summary we describe the design, production, and initial testing of a multi-functional, targeted delivery technology platform based on a highly engineered HBc VLP. Initial platform versatility and efficacy is demonstrated by efficient cargo loading (> 85%) and surface conjugation (> 95%) of multiple agents, important requirements for any effective targeting platform (Figures 3, 4D, and 4E). Furthermore, we show that our innovative process using CFPS, anaerobic Ni-NTA purification and two-step assembly achieves 6 x 10^{13} NPs per mL of CFPS reaction; approximately 100-fold higher than current AAV yields[72,73] and approximately 8x more than any previously reported HBc VLP yields either from cell-free or *in vivo* production.[35–39]

To achieve this, the speed, convenience, and control offered by CFPS proved to be highly beneficial, if not essential, for project success. Protein production in a low ionic strength environment, an option not available *in vivo*, was easily accomplished and highly effective in producing unassembled HBc proteins (Figures 2A–2C). This avoided the need for the disassembly and reassembly sequence often used for HBc VLP production.[50,65,74,75] Instead, high yield anaerobic Ni-NTA purification could be performed without harsh denaturing conditions (Figures 2D–2H) as was previously necessary.[38,51] As anaerobic processing is a well-established chemical engineering capability, it becomes easier as the scale is increased and should not raise concerns regarding scalability.[76] Further, we show that the versatility of CFPS also facilitated the production of surface adducts such as a viral antigen potentially capable of eliciting highly protective immune responses. Such antigens often are subdomains of much larger proteins. Since these domains typically expose hydrophobic, previously buried surfaces, low ionic strength, and low expression temperatures as well as modest concentrations of a selective surfactant and/or chaperons can be highly beneficial (Figure 4B), again remedies not available with *in vivo* production. Additionally, CFPS could prove to be beneficial for the expression and processing of other NPs, such as encapsulins.[77]

The other critical advantage of CFPS is the facile incorporation of non-natural amino acids. Site-specific incorporation of non-natural amino acids, in our case displaying orthogonally reactive moieties, allows versatile surface functionalization with minimal impact on protein folding and VLP assembly efficiency. Simply mutating the sole methionine to serine and introducing the

ATG codon at either position 76 or 80 enabled attachment of properly orientated and fully accessible adducts as evidenced by recognition of the Dengue fever antigen by a neutralizing antibody (Figure 4H) and variations in the pharmacokinetic profiles offered by attaching different amounts of PEG (Figure 5A).

Initially, however, many of our first approaches for surface conjugation were problematic. We began by anaerobically performing copper-catalyzed azide-alkyne click reactions using published activator molecules.[78] While conjugation was achieved, SDS gel analysis revealed protein damage as well as low conjugation efficiency. Direct use of DBCO linkers avoided the damage but also suffered from low attachment frequency (Figure S3). Finally, robust results were obtained by combining SPAAC and maleimide conjugation with inverse—demand Diels-Alder cycloaddition [68] via bifunctional linkers (Figure 4). Reliable and efficient surface attachment was achieved, crucial for both future targeted delivery of therapeutics as well as vaccine efficacy to ensure effective targeting and minimize immune responses against the HBc protein itself. Many previous studies have also sought to provide HBc VLP surface functionality through polypeptide fusions,[35,79–81] while more recent studies have used the SpyCatcher system.[39,52,82] The impact of polypeptide fusions on subunit folding as well as VLP assembly and stability[83] and possible SpyCatcher system immunogenicity[52] raise concerns. Furthermore, the SpyCatcher system requires the fusion of a 13 amino acid tag to potential adducts which can also be problematic and laborious.[52] In contrast, site-specific conjugation is flexible, fast, and raises minimal concerns regarding added immunogenicity.

Another major prerequisite for any effective targeting platform besides efficient production and surface functionalization is the ability to load and co-load multiple types of cargoes. While previous studies have demonstrated successful cargo loading of a set of diverse molecules for different VLP platforms using different methods,[14–17,19,84] the two most common approaches for HBc VLP loading have limitations. Specifically, both the disassembly-reassembly process[49,50] and thermally triggered expansion of the HBc VLPs pores to allow cargo diffusion into the VLPs[74,85,86] expose the VLPs to either harsh denaturing conditions or potentially deleterious high temperature. Furthermore, work by us and others[65] has shown that small molecular cargoes can diffuse out of the VLP after initial loading if not retained by a covalent bond. A more recent report demonstrates the ability to load GFP by attaching it to a capsid assembly modulator. [75] However, this approach also displays cargo on the VLP surface requiring an additional cleavage step to remove the exposed cargo. Furthermore, it necessitates attaching the capsid assembly modulator to the cargo and is therefore more challenging to adapt for non-protein cargoes. In comparison, we show that the hydrophobic, sulfide-presenting loading domain that presumably coats the inside surface of the VLP is capable of loading and retaining several different types of cargoes: an anti-cancer toxin, a fluorophore, DNA and a protein (Figure 3; Table 1). High loading efficiency (> 85%) is achieved via rapid, irreversible maleimide conjugation that covalently captures and retains the cargo during assembly. However, the loading efficiency is significantly decreased when forming the reversible disulfide bond formation under anaerobic conditions as evidenced by achieving only ca. 7% loading for mertansine. In this case, the covalent tethering is not effected until the disulfide bond forming H_2O_2 treatment is conducted after assembly is completed. This delay results in a ca. 80-fold decrease in cargo condensation during loading compared to that achieved with maleimide. Yet, the 176-fold internal mertansine condensation is still impressive, most likely due to the intrinsic hydrophobicity of the molecule; especially since mertansine addition followed AF750M loading which most likely already occupied many of the loading domains.

We believe that the C-terminal loading domain is not only essential for cargo loading but might also alter the mechanism of assembly. Previous work with HBc 1-149 amino acids suggested that assembly proceeds with initial tetrameric and hexameric intermediates.[48,59] We hypothesize that the potential self-association of the hydrophobic loading domains suggested by our purification results could be stimulating the formation of larger assembly intermediates, possibly plates with pentameric and hexameric symmetries. These larger intermediates could then catalyze more efficient VLP assembly.

While the initial requirements for an effective targeting platform have been validated, future studies will need to demonstrate endosomal escape via the proton sponge effect facilitated by the 240 C-terminal HisTags associated with each VLP (1440 additional histidines), as other studies have demonstrated for different histidine rich constructs.[87–90] Furthermore, immune system avoidance for therapies other than vaccines needs to be improved by either providing different surface pegylation or by other approaches.[91–94]

Finally, effective cellular and *in vivo* targeting using nanobodies, single chain variable fragments or other targeting ligands needs to be demonstrated.

Repeatedly, we found that discerning quality control assays for each process step were essential and now provide a solid foundation for process validation to support subsequent preparation of investigational new drug (IND) applications for FDA submission. These assays are summarized in Table 2. Importantly, the 3-month 4°C stability of the VLPs can greatly accelerate product development by providing a convenient "inventoried" intermediate. For example, 3 to 4 VLP candidates, each with different combinations of loaded cargo molecules, could first be prepared in parallel. Each of these would then be surface functionalized with different candidate targeting ligands and either immune system avoidance or stimulation adducts. This family of product candidates could then be evaluated either sequentially or in parallel in cell-based and animal models to determine relative efficacies. If one of the cargo molecules or surface attached ligands were an appropriate fluorophore, cell and whole-body imaging could compare targeting efficiency to overall efficacy and, if present, severity of side effects.

In the graphical abstract, we suggest four different applications for our platform. It is also intriguing to consider combinations. In particular, a targeted cancer therapeutic VLP that is also loaded with a near infrared fluorophore could enable rapid evaluation of the extent of metastasis while also providing an effective treatment. We also recognize that this VLP production platform is likely to have many other applications beyond those suggested by our graphical abstract.

Table 2. Quality assessment after every production step outlined for both the HBc VLP and surface adducts

Product	Production step	Quality control assay	Parameter
HBc VLP	Production (CFPS)	SDS-PAGE/autoradiogram	Protein size
		Liquid scintillation counting	Expression yield
	Purification (Ni-NTA)	SDS-PAGE	Purity
		Protein assay after imidazole removal	Purification yield
	VLP assembly	SEC A280 chromatogram	Assembly efficiency
		DLS	Particle size and purity
	Cargo loading	sfGFP and fluorophores: fluorescence analysis	Loading efficiency
		Mertansine: HPLC	
		CpG DNA: SDS-PAGE	
	Conjugation	SDS-PAGE	Size and conjugation efficiency
		DLS	Particle size and purity
Surface adducts (*e.g.*, antigen)	Production (CFPS)	Autoradiogram	Protein size
		Liquid scintillation counting	Expression yield
	Purification (Ni-NTA)	SDS-PAGE	Purity
		Protein assay after imidazole removal	Purification yield
	Functionality after attachment	Immunoprecipitation via neutralizing antibody	Correct display of antigen

Conclusion

In summary, we report an HBc VLP design and production process using a highly engineered HBc protein to provide stabilized, multifunctional, and versatile VLPs. These NPs offer a 26 nm diameter hollow chamber for loading small as well as large molecular weight cargoes and can be surface modified to provide a variety of functionalities. The process provides NPs with high purity and quality at yields of approximately 6 x 10^{13} NPs per mL of CFPS reaction: about eight times that of the best previously published procedure.[35–39]

Limitations of the study

The focus of this paper was to establish a delivery platform with a high yielding and reliable manufacturing process. Further validation is needed to assess performance of the VLPs *in vivo*. This includes successful cell targeting and verification of endosomal escape after internalization by the targeted cells. Although increased PEGylation lead to longer *in vivo* circulation, more efficient liver avoidance would be highly beneficial.

RESOURCE AVAILABILITY

Lead contact

James R. Swartz (jswartz@stanford.edu).

Materials availability

All methods for materials produced in this study are outlined in the STAR Methods section.

Data and code availability

- This study did not create any code and all data needed to interpret the results is available in the manuscript including standard deviation of detailed data and number of repeats.
- If any additional information is needed, please reach out to the lead contact.
- All (raw) data reported in the manuscript are available from the lead contact upon request.

ACKNOWLEDGMENTS

We thank former Swartz lab members Maya Nagasawa, Julie Fogarty, Marcus Rohovie, Rinchu Mathew, and Max Levine for their contributions to this work. The TEM imaging was performed at the Stanford Nano Shared Facilities (SNSF), and we are grateful to Pinaki Mukherjee for assistance with TEM Imaging. We also thank Rochelle Aw and the Jewett Lab for providing us with their DsbC protocol. We have no funding sources to declare.

AUTHOR CONTRIBUTIONS

Conceptualization: A.S.R. and J.R.S.; methodology: A.S.R., M.N., and J.R.S.; validation: A.S.R., M.N., and P.E.J.S.; formal analysis: A.S.R.; investigation: A.S.R., M.N., and P.E.J.S.; resources: A.S.R., M.N., and P.E.J.S.; writing – original draft: A.S.R. and J.R.S.; writing – review and editing: A.S.R., M.N., P.E.J.S., and J.R.S.; visualization: A.S.R.; supervision: A.S.R. and J.R.S.; funding acquisition: J.R.S.

DECLARATION OF INTERESTS

J.R.S. is co-founder and has an ownership share in a small virtual company called VLP Delivery, Inc. J.R.S. is an inventor of two patents owned by Stanford University and Licensed to VLP Delivery, Inc.: (1) Engineered Hepatitis B core polypeptide (US11,261,216) and (2) Optimized Hepatitis B core (HBc) and VLPs (US9,896,483).

STAR★METHODS

Detailed methods are provided in the online version of this paper and include the following:

- KEY RESOURCES TABLE
- EXPERIMENTAL MODEL AND SUBJECT DETAILS
- METHOD DETAILS
  - Materials

SUPPLEMENTAL INFORMATION

Supplemental information can be found online at https://doi.org/10.1016/j.isci.2025.112599.

Received: November 22, 2024
Revised: January 20, 2025
Accepted: May 2, 2025
Published: May 7, 2025

REFERENCES

1. Schwartz, R.S. (2004). Paul Ehrlich's magic bullets. N. Engl. J. Med. *350*, 1079–1080. https://doi.org/10.1056/NEJMp048021.
2. Lyu, P., and Lu, B. (2022). New Advances in Using Virus-like Particles and Related Technologies for Eukaryotic Genome Editing Delivery. Int. J. Mol. Sci. *23*, 8750. https://doi.org/10.3390/ijms23158750.
3. Rohovie, M.J., Nagasawa, M., and Swartz, J.R. (2017). Virus-like particles: Next-generation nanoparticles for targeted therapeutic delivery. Bioeng. Transl. Med. *2*, 43–57. https://doi.org/10.1002/btm2.10049.
4. Madigan, V., Zhang, F., and Dahlman, J.E. (2023). Drug delivery systems for CRISPR-based genome editors. Nat. Rev. Drug Discov. *22*, 875–894. https://doi.org/10.1038/s41573-023-00762-x.
5. Nooraei, S., Bahrulolum, H., Hoseini, Z.S., Katalani, C., Hajizade, A., Easton, A.J., and Ahmadian, G. (2021). Virus-like particles: preparation, immunogenicity and their roles as nanovaccines and drug nanocarriers. J. Nanobiotechnol. *19*, 59. https://doi.org/10.1186/s12951-021-00806-7.
6. Teunissen, E.A., de Raad, M., and Mastrobattista, E. (2013). Production and biomedical applications of virus-like particles derived from polyomaviruses. J. Control. Release *172*, 305–321. https://doi.org/10.1016/j.jconrel.2013.08.026.
7. Martins, S.A., Santos, J., Silva, R.D.M., Rosa, C., Cabo Verde, S., Correia, J.D.G., and Melo, R. (2022). How promising are HIV-1-based virus-like particles for medical applications. Front. Cell. Infect. Microbiol. *12*, 997875. https://doi.org/10.3389/fcimb.2022.997875.
8. Beatty, P.H., and Lewis, J.D. (2019). Cowpea mosaic virus nanoparticles for cancer imaging and therapy. Adv. Drug Deliv. Rev. *145*, 130–144. https://doi.org/10.1016/j.addr.2019.04.005.
9. Wang, J.H., Gessler, D.J., Zhan, W., Gallagher, T.L., and Gao, G. (2024). Adeno-associated virus as a delivery vector for gene therapy of human diseases. Signal Transduct. Target. Ther. *9*, 78. https://doi.org/10.1038/s41392-024-01780-w.
10. Wynne, S.A., Crowther, R.A., and Leslie, A.G. (1999). The crystal structure of the human hepatitis B virus capsid. Mol. Cell *3*, 771–780. https://doi.org/10.1016/s1097-2765(01)80009-5.
11. Yang, D., Chen, L., Duan, J., Yu, Y., Zhou, J., and Lu, H. (2021). Investigation of Kluyveromyces marxianus as a novel host for large-scale production of porcine parvovirus virus-like particles. Microb. Cell Fact. *20*, 24. https://doi.org/10.1186/s12934-021-01514-5.
12. Lua, L.H.L., Connors, N.K., Sainsbury, F., Chuan, Y.P., Wibowo, N., and Middelberg, A.P.J. (2014). Bioengineering virus-like particles as vaccines. Biotechnol. Bioeng. *111*, 425–440. https://doi.org/10.1002/bit.25159.
13. Cervera, L., González-Domínguez, I., Segura, M.M., and Gòdia, F. (2017). Intracellular characterization of Gag VLP production by transient transfection of HEK 293 cells. Biotechnol. Bioeng. *114*, 2507–2517. https://doi.org/10.1002/bit.26367.
14. Sun, X., Li, W., Zhang, X., Qi, M., Zhang, Z., Zhang, X.E., and Cui, Z. (2016). In Vivo Targeting and Imaging of Atherosclerosis Using Multifunctional Virus-Like Particles of Simian Virus 40. Nano Lett. *16*, 6164–6171. https://doi.org/10.1021/acs.nanolett.6b02386.
15. Plummer, E.M., and Manchester, M. (2013). Endocytic uptake pathways utilized by CPMV nanoparticles. Mol. Pharm. *10*, 26–32. https://doi.org/10.1021/mp300238w.
16. Lico, C., Tanno, B., Marchetti, L., Novelli, F., Giardullo, P., Arcangeli, C., Pazzaglia, S., Podda, M.S., Santi, L., Bernini, R., et al. (2021). Tomato Bushy Stunt Virus Nanoparticles as a Platform for Drug Delivery to Shh-Dependent Medulloblastoma. Int. J. Mol. Sci. *22*, 10523. https://doi.org/10.3390/ijms221910523.
17. Kato, T., Yui, M., Deo, V.K., and Park, E.Y. (2015). Development of Rous sarcoma Virus-like Particles Displaying hCC49 scFv for Specific Targeted Drug Delivery to Human Colon Carcinoma Cells. Pharm. Res. *32*, 3699–3707. https://doi.org/10.1007/s11095-015-1730-2.
18. McNeale, D., Dashti, N., Cheah, L.C., and Sainsbury, F. (2023). Protein cargo encapsulation by virus-like particles: Strategies and applications. Wiley Interdiscip. Rev. Nanomed. Nanobiotechnol. *15*, e1869. https://doi.org/10.1002/wnan.1869.
19. Grataitong, K., Huault, S., Chotwiwatthanakun, C., Jariyapong, P., Thongsum, O., Chawiwithaya, C., Chakrabandhu, K., Hueber, A.O., and Weerachatyanukul, W. (2021). Chimeric virus-like particles (VLPs) designed from shrimp nodavirus (MrNV) capsid protein specifically target EGFR-positive human colorectal cancer cells. Sci. Rep. *11*, 16579. https://doi.org/10.1038/s41598-021-95891-x.
20. Lizatovic, R., Assent, M., Barendregt, A., Dahlin, J., Bille, A., Satzinger, K., Tupina, D., Heck, A.J.R., Wennmalm, S., and Andre, I. (2018). A Protein-Based Encapsulation System with Calcium-Controlled Cargo Loading and Detachment. Angew Chem. Int. Ed. Engl. *57*, 11334–11338. https://doi.org/10.1002/anie.201806466.
21. Molino, N.M., Anderson, A.K.L., Nelson, E.L., and Wang, S.W. (2013). Biomimetic protein nanoparticles facilitate enhanced dendritic cell activation and cross-presentation. ACS Nano *7*, 9743–9752. https://doi.org/10.1021/nn403085w.
22. Lu, Y., Chan, W., Ko, B.Y., VanLang, C.C., and Swartz, J.R. (2015). Assessing sequence plasticity of a virus-like nanoparticle by evolution toward a versatile scaffold for vaccines and drug delivery. Proc. Natl. Acad. Sci. USA *112*, 12360–12365. https://doi.org/10.1073/pnas.1510533112.
23. Bundy, B.C., and Swartz, J.R. (2011). Efficient disulfide bond formation in virus-like particles. J. Biotechnol. *154*, 230–239. https://doi.org/10.1016/j.jbiotec.2011.04.011.
24. Dong, H., Lu, Y., Zhang, Y., Mu, S., Wang, N., Du, P., Zhi, X., Wen, X., Wang, X., Sun, S., et al. (2021). A Heat-Induced Mutation on VP1 of Foot-and-Mouth Disease Virus Serotype O Enhanced Capsid Stability and Immunogenicity. J. Virol. *95*, e0017721. https://doi.org/10.1128/JVI.00177-21.

25. Marsian, J., Fox, H., Bahar, M.W., Kotecha, A., Fry, E.E., Stuart, D.I., Macadam, A.J., Rowlands, D.J., and Lomonossoff, G.P. (2017). Plant-made polio type 3 stabilized VLPs-a candidate synthetic polio vaccine. Nat. Commun. *8*, 245. https://doi.org/10.1038/s41467-017-00090-w.

26. Crooke, S.N., Zheng, J., Ganewatta, M.S., Guldberg, S.M., Reineke, T.M., and Finn, M.G. (2019). Immunological Properties of Protein-Polymer Nanoparticles. ACS Appl. Bio Mater. *2*, 93–103. https://doi.org/10.1021/acsabm.8b00418.

27. Eto, Y., Yoshioka, Y., Ishida, T., Yao, X., Morishige, T., Narimatsu, S., Mizuguchi, H., Mukai, Y., Okada, N., Kiwada, H., and Nakagawa, S. (2010). Optimized PEGylated adenovirus vector reduces the anti-vector humoral immune response against adenovirus and induces a therapeutic effect against metastatic lung cancer. Biol. Pharm. Bull. *33*, 1540–1544. https://doi.org/10.1248/bpb.33.1540.

28. Toy, R., Hayden, E., Camann, A., Berman, Z., Vicente, P., Tran, E., Meyers, J., Pansky, J., Peiris, P.M., Wu, H., et al. (2013). Multimodal in vivo imaging exposes the voyage of nanoparticles in tumor microcirculation. ACS Nano *7*, 3118–3129. https://doi.org/10.1021/nn3053439.

29. Guo, X., Wu, Z., Li, W., Wang, Z., Li, Q., Kong, F., Zhang, H., Zhu, X., Du, Y. P., Jin, Y., et al. (2016). Appropriate Size of Magnetic Nanoparticles for Various Bioapplications in Cancer Diagnostics and Therapy. ACS Appl. Mater. Interfaces *8*, 3092–3106. https://doi.org/10.1021/acsami.5b10352.

30. Ashley, C.E., Carnes, E.C., Phillips, G.K., Durfee, P.N., Buley, M.D., Lino, C.A., Padilla, D.P., Phillips, B., Carter, M.B., Willman, C.L., et al. (2011). Cell-specific delivery of diverse cargos by bacteriophage MS2 virus-like particles. ACS Nano *5*, 5729–5745. https://doi.org/10.1021/nn201397z.

31. Biabanikhankahdani, R., Alitheen, N.B.M., Ho, K.L., and Tan, W.S. (2016). pH-responsive Virus-like Nanoparticles with Enhanced Tumour-targeting Ligands for Cancer Drug Delivery. Sci. Rep. *6*, 37891. https://doi.org/10.1038/srep37891.

32. Lino, C.A., Caldeira, J.C., and Peabody, D.S. (2017). Display of single-chain variable fragments on bacteriophage MS2 virus-like particles. J. Nanobiotechnol. *15*, 13. https://doi.org/10.1186/s12951-016-0240-7.

33. Blanco, E., Shen, H., and Ferrari, M. (2015). Principles of nanoparticle design for overcoming biological barriers to drug delivery. Nat. Biotechnol. *33*, 941–951. https://doi.org/10.1038/nbt.3330.

34. Wynne, S.A., Leslie, A.G., Butler, P.J., and Crowther, R.A. (1999). Crystallization of hepatitis B virus core protein shells: determination of cryoprotectant conditions and preliminary X-ray characterization. Acta Crystallogr. D Biol. Crystallogr. *55*, 557–560. https://doi.org/10.1107/s0907444998012621.

35. Mohamed Suffian, I.F.B., Wang, J.T.W., Hodgins, N.O., Klippstein, R., Garcia-Maya, M., Brown, P., Nishimura, Y., Heidari, H., Bals, S., Sosabowski, J.K., et al. (2017). Engineering hepatitis B virus core particles for targeting HER2 receptors in vitro and in vivo. Biomaterials *120*, 126–138. https://doi.org/10.1016/j.biomaterials.2016.12.012.

36. Zhang, Y., Liu, Y., Zhang, B., Yin, S., Li, X., Zhao, D., Wang, W., Bi, J., and Su, Z. (2021). In vitro preparation of uniform and nucleic acid free hepatitis B core particles through an optimized disassembly-purification-reassembly process. Protein Expr. Purif. *178*, 105747. https://doi.org/10.1016/j.pep.2020.105747.

37. Arora, U., Tyagi, P., Swaminathan, S., and Khanna, N. (2012). Chimeric Hepatitis B core antigen virus-like particles displaying the envelope domain III of dengue virus type 2. J. Nanobiotechnol. *10*, 30. https://doi.org/10.1186/1477-3155-10-30.

38. Bin Mohamed Suffian, I.F., Garcia-Maya, M., Brown, P., Bui, T., Nishimura, Y., Palermo, A.R.B.M.J., Ogino, C., Kondo, A., and Al-Jamal, K.T. (2017). Yield Optimisation of Hepatitis B Virus Core Particles in E. coli Expression System for Drug Delivery Applications. Sci. Rep. *7*, 43160. https://doi.org/10.1038/srep43160.

39. Marini, A., Zhou, Y., Li, Y., Taylor, I.J., Leneghan, D.B., Jin, J., Zaric, M., Mekhaiel, D., Long, C.A., Miura, K., and Biswas, S. (2019). A Universal Plug-and-Display Vaccine Carrier Based on HBsAg VLP to Maximize Effective Antibody Response. Front. Immunol. *10*, 2931. https://doi.org/10.3389/fimmu.2019.02931.

40. Spice, A.J., Aw, R., Bracewell, D.G., and Polizzi, K.M. (2020). Synthesis and Assembly of Hepatitis B Virus-Like Particles in a Pichia pastoris Cell-Free System. Front. Bioeng. Biotechnol. *8*, 72. https://doi.org/10.3389/fbioe.2020.00072.

41. Colant, N., Melinek, B., Frank, S., Rosenberg, W., and Bracewell, D.G. (2021). Escherichia Coli-Based Cell-Free Protein Synthesis for Iterative Design of Tandem-Core Virus-Like Particles. Vaccines (Basel) *9*, 193. https://doi.org/10.3390/vaccines9030193.

42. Jewett, M.C., and Swartz, J.R. (2004). Mimicking the Escherichia coli cytoplasmic environment activates long-lived and efficient cell-free protein synthesis. Biotechnol. Bioeng. *86*, 19–26. https://doi.org/10.1002/bit.20026.

43. Kim, D.M., and Swartz, J.R. (2004). Efficient production of a bioactive, multiple disulfide-bonded protein using modified extracts of Escherichia coli. Biotechnol. Bioeng. *85*, 122–129. https://doi.org/10.1002/bit.10865.

44. Hunt, A.C., Rasor, B.J., Seki, K., Ekas, H.M., Warfel, K.F., Karim, A.S., and Jewett, M.C. (2025). Cell-Free Gene Expression: Methods and Applications. Chem. Rev. *125*, 91–149. https://doi.org/10.1021/acs.chemrev.4c00116.

45. Carlson, E.D., Gan, R., Hodgman, C.E., and Jewett, M.C. (2012). Cell-free protein synthesis: applications come of age. Biotechnol. Adv. *30*, 1185–1194. https://doi.org/10.1016/j.biotechadv.2011.09.016.

46. Zawada, J.F., Yin, G., Steiner, A.R., Yang, J., Naresh, A., Roy, S.M., Gold, D.S., Heinsohn, H.G., and Murray, C.J. (2011). Microscale to manufacturing scale-up of cell-free cytokine production–a new approach for shortening protein production development timelines. Biotechnol. Bioeng. *108*, 1570–1578. https://doi.org/10.1002/bit.23103.

47. Hunt, J.P., Yang, S.O., Wilding, K.M., and Bundy, B.C. (2017). The growing impact of lyophilized cell-free protein expression systems. Bioengineered *8*, 325–330. https://doi.org/10.1080/21655979.2016.1241925.

48. Zlotnick, A., Johnson, J.M., Wingfield, P.W., Stahl, S.J., and Endres, D. (1999). A theoretical model successfully identifies features of hepatitis B virus capsid assembly. Biochemistry *38*, 14644–14652. https://doi.org/10.1021/bi991611a.

49. Shan, W., Chen, R., Zhang, Q., Zhao, J., Chen, B., Zhou, X., Ye, S., Bi, S., Nie, L., and Ren, L. (2018). Improved Stable Indocyanine Green (ICG)-Mediated Cancer Optotheranostics with Naturalized Hepatitis B Core Particles. Adv. Mater. *30*, e1707567. https://doi.org/10.1002/adma.201707567.

50. Suffian, I.F.M., Wang, J.T.W., Faruqu, F.N., Benitez, J., Nishimura, Y., Ogino, C., Kondo, A., and Al-Jamal, K.T. (2018). Engineering Human Epidermal Growth Receptor 2-Targeting Hepatitis B Virus Core Nanoparticles for siRNA Delivery in Vitro and in Vivo. ACS Appl. Nano Mater. *1*, 3269–3282. https://doi.org/10.1021/acsanm.8b00480.

51. Wizemann, H., and von Brunn, A. (1999). Purification of E. coli-expressed HIS-tagged hepatitis B core antigen by Ni2+ -chelate affinity chromatography. J. Virol. Methods *77*, 189–197. https://doi.org/10.1016/s0166-0934(98)00152-9.

52. Hatlem, D., Trunk, T., Linke, D., and Leo, J.C. (2019). Catching a SPY: Using the SpyCatcher-SpyTag and Related Systems for Labeling and Localizing Bacterial Proteins. Int. J. Mol. Sci. *20*, 2129. https://doi.org/10.3390/ijms20092129.

53. Epstein, W. (2003). The roles and regulation of potassium in bacteria. Prog. Nucleic Acid Res. Mol. Biol. *75*, 293–320. https://doi.org/10.1016/s0079-6603(03)75008-9.

54. Bennett, B.D., Kimball, E.H., Gao, M., Osterhout, R., Van Dien, S.J., and Rabinowitz, J.D. (2009). Absolute metabolite concentrations and implied enzyme active site occupancy in Escherichia coli. Nat. Chem. Biol. *5*, 593–599. https://doi.org/10.1038/nchembio.186.

55. Dopp, B.J.L., Tamiev, D.D., and Reuel, N.F. (2019). Cell-free supplement mixtures: Elucidating the history and biochemical utility of additives

used to support in vitro protein synthesis in E. coli extract. Biotechnol. Adv. *37*, 246–258. https://doi.org/10.1016/j.biotechadv.2018.12.006.

56. Crowther, R.A., Kiselev, N.A., Böttcher, B., Berriman, J.A., Borisova, G.P., Ose, V., and Pumpens, P. (1994). Three-dimensional structure of hepatitis B virus core particles determined by electron cryomicroscopy. Cell *77*, 943–950. https://doi.org/10.1016/0092-8674(94)90142-2.

57. Selzer, L., Katen, S.P., and Zlotnick, A. (2014). The hepatitis B virus core protein intradimer interface modulates capsid assembly and stability. Biochemistry *53*, 5496–5504. https://doi.org/10.1021/bi500732b.

58. Handlon, A.L., and Oppenheimer, N.J. (1988). Thiol reduction of 3'-azidothymidine to 3'-aminothymidine: kinetics and biomedical implications. Pharm. Res. *5*, 297–299. https://doi.org/10.1023/a:1015926720740.

59. Oliver, R.C., Potrzebowski, W., Najibi, S.M., Pedersen, M.N., Arleth, L., Mahmoudi, N., and André, I. (2020). Assembly of Capsids from Hepatitis B Virus Core Protein Progresses through Highly Populated Intermediates in the Presence and Absence of RNA. ACS Nano *14*, 10226–10238. https://doi.org/10.1021/acsnano.0c03569.

60. Pavlova, A., Bassit, L., Cox, B.D., Korablyov, M., Chipot, C., Patel, D., Lynch, D.L., Amblard, F., Schinazi, R.F., and Gumbart, J.C. (2022). The Mechanism of Action of Hepatitis B Virus Capsid Assembly Modulators Can Be Predicted from Binding to Early Assembly Intermediates. J. Med. Chem. *65*, 4854–4864. https://doi.org/10.1021/acs.jmedchem.1c02040.

61. Katen, S.P., Chirapu, S.R., Finn, M.G., and Zlotnick, A. (2010). Trapping of hepatitis B virus capsid assembly intermediates by phenylpropenamide assembly accelerators. ACS Chem. Biol. *5*, 1125–1136. https://doi.org/10.1021/cb100275b.

62. Xie, Q., Bu, W., Bhatia, S., Hare, J., Somasundaram, T., Azzi, A., and Chapman, M.S. (2002). The atomic structure of adeno-associated virus (AAV-2), a vector for human gene therapy. Proc. Natl. Acad. Sci. USA *99*, 10405–10410. https://doi.org/10.1073/pnas.162250899.

63. DiMattia, M.A., Nam, H.J., Van Vliet, K., Mitchell, M., Bennett, A., Gurda, B. L., McKenna, R., Olson, N.H., Sinkovits, R.S., Potter, M., et al. (2012). Structural insight into the unique properties of adeno-associated virus serotype 9. J. Virol. *86*, 6947–6958. https://doi.org/10.1128/JVI.07232-11.

64. Xie, Q., Yoshioka, C.K., and Chapman, M.S. (2020). Adeno-Associated Virus (AAV-DJ)-Cryo-EM Structure at 1.56 A Resolution. Viruses *12*, 1194. https://doi.org/10.3390/v12101194.

65. Shan, W., Zhang, D., Wu, Y., Lv, X., Hu, B., Zhou, X., Ye, S., Bi, S., Ren, L., and Zhang, X. (2018). Modularized peptides modified HBc virus-like particles for encapsulation and tumor-targeted delivery of doxorubicin. Nanomedicine *14*, 725–734. https://doi.org/10.1016/j.nano.2017.12.002.

66. Meredith, S.A., Kusunoki, Y., Connell, S.D., Morigaki, K., Evans, S.D., and Adams, P.G. (2023). Self-Quenching Behavior of a Fluorescent Probe Incorporated within Lipid Membranes Explored Using Electrophoresis and Fluorescence Lifetime Imaging Microscopy. J. Phys. Chem. B *127*, 1715–1727. https://doi.org/10.1021/acs.jpcb.2c07652.

67. Renner, M., Flanagan, A., Dejnirattisai, W., Puttikhunt, C., Kasinrerk, W., Supasa, P., Wongwiwat, W., Chawansuntati, K., Duangchinda, T., Cowper, A., et al. (2018). Characterization of a potent and highly unusual minimally enhancing antibody directed against dengue virus. Nat. Immunol. *19*, 1248–1256. https://doi.org/10.1038/s41590-018-0227-7.

68. Blackman, M.L., Royzen, M., and Fox, J.M. (2008). Tetrazine ligation: fast bioconjugation based on inverse-electron-demand Diels-Alder reactivity. J. Am. Chem. Soc. *130*, 13518–13519. https://doi.org/10.1021/ja8053805.

69. Harrell, M.I., Iritani, B.M., and Ruddell, A. (2008). Lymph node mapping in the mouse. J. Immunol. Methods *332*, 170–174. https://doi.org/10.1016/j.jim.2007.11.012.

70. Simonsen, J.B., and Kromann, E.B. (2021). Pitfalls and opportunities in quantitative fluorescence-based nanomedicine studies - A commentary. J. Control. Release *335*, 660–667. https://doi.org/10.1016/j.jconrel.2021.05.041.

71. Jin, K.T., Yao, J.Y., Ying, X.J., Lin, Y., and Chen, Y.F. (2020). Nanomedicine and Early Cancer Diagnosis: Molecular Imaging using Fluorescence Nanoparticles. Curr. Top. Med. Chem. *20*, 2737–2761. https://doi.org/10.2174/1568026620666200922112640.

72. Coplan, L., Zhang, Z., Ragone, N., Reeves, J., Rodriguez, A., Shevade, A., Bak, H., and Tustian, A.D. (2024). High-yield recombinant adeno-associated viral vector production by multivariate optimization of bioprocess and transfection conditions. Biotechnol. Prog. *40*, e3445. https://doi.org/10.1002/btpr.3445.

73. Zhao, H., Lee, K.J., Daris, M., Lin, Y., Wolfe, T., Sheng, J., Plewa, C., Wang, S., and Meisen, W.H. (2020). Creation of a High-Yield AAV Vector Production Platform in Suspension Cells Using a Design-of-Experiment Approach. Mol. Ther. Methods Clin. Dev. *18*, 312–320. https://doi.org/10.1016/j.omtm.2020.06.004.

74. Wei, J., Li, Z., Yang, Y., Ma, X., An, W., Ma, G., Su, Z., and Zhang, S. (2020). A biomimetic VLP influenza vaccine with interior NP/exterior M2e antigens constructed through a temperature shift-based encapsulation strategy. Vaccine *38*, 5987–5996. https://doi.org/10.1016/j.vaccine.2020.07.015.

75. Hussain, T., Zhao, Z., Murphy, B., Taylor, Z.E., Gudorf, J.A., Klein, S., Barnes, L.F., VanNieuwenhze, M., Jarrold, M.F., and Zlotnick, A. (2024). Chemically Tagging Cargo for Specific Packaging inside and on the Surface of Virus-like Particles. ACS Nano *18*, 21024–21037. https://doi.org/10.1021/acsnano.4c02056.

76. Zhao, Z., Li, Y., Zhang, Y., and Lovley, D.R. (2020). Sparking Anaerobic Digestion: Promoting Direct Interspecies Electron Transfer to Enhance Methane Production. iScience *23*, 101794. https://doi.org/10.1016/j.isci.2020.101794.

77. Jones, J.A., and Giessen, T.W. (2021). Advances in encapsulin nanocompartment biology and engineering. Biotechnol. Bioeng. *118*, 491–505. https://doi.org/10.1002/bit.27564.

78. Soriano Del Amo, D., Wang, W., Jiang, H., Besanceney, C., Yan, A.C., Levy, M., Liu, Y., Marlow, F.L., and Wu, P. (2010). Biocompatible copper (I) catalysts for in vivo imaging of glycans. J. Am. Chem. Soc. *132*, 16893–16899. https://doi.org/10.1021/ja106553e.

79. Lei, L., Qin, H., Luo, J., Tan, Y., Yang, J., and Pan, Z. (2021). Construction and immunological evaluation of hepatitis B virus core virus-like particles containing multiple antigenic peptides of respiratory syncytial virus. Virus Res. *298*, 198410. https://doi.org/10.1016/j.virusres.2021.198410.

80. Sazegari, S., Akbarzadeh Niaki, M., Afsharifar, A., Niazi, A., Derakhshandeh, A., Moradi Vahdat, M., Hemmati, F., and Eskandari, M.H. (2023). Chimeric Hepatitis B core virus-like particles harboring SARS-CoV2 epitope elicit a humoral immune response in mice. Microb. Cell Fact. *22*, 39. https://doi.org/10.1186/s12934-023-02043-z.

81. Cheng, K., Du, T., Li, Y., Qi, Y., Min, H., Wang, Y., Zhang, Q., Wang, C., Zhou, Y., Li, L., et al. (2020). Dual-Antigen-Loaded Hepatitis B Virus Core Antigen Virus-like Particles Stimulate Efficient Immunotherapy Against Melanoma. ACS Appl. Mater. Interfaces *12*, 53682–53690. https://doi.org/10.1021/acsami.0c16012.

82. Hartzell, E.J., Lieser, R.M., Sullivan, M.O., and Chen, W. (2020). Modular Hepatitis B Virus-like Particle Platform for Biosensing and Drug Delivery. ACS Nano *14*, 12642–12651. https://doi.org/10.1021/acsnano.9b08756.

83. Hill, B.D., Zak, A., Khera, E., and Wen, F. (2018). Engineering Virus-like Particles for Antigen and Drug Delivery. Curr. Protein Pept. Sci. *19*, 112–127. https://doi.org/10.2174/1389203718666161122113041.

84. Esquirol, L., McNeale, D., Douglas, T., Vickers, C.E., and Sainsbury, F. (2022). Rapid Assembly and Prototyping of Biocatalytic Virus-like Particle Nanoreactors. ACS Synth. Biol. *11*, 2709–2718. https://doi.org/10.1021/acssynbio.2c00117.

85. Lu, F., Li, Z., Sheng, Y., Ma, Y., Yang, Y., Ren, Y., Su, Z., Yu, R., and Zhang, S. (2021). Thermal-triggered packing of lipophilic NIR dye IR780 in hepatitis B core at critical ionic strength and cargo-host ratio for improved stability and enhanced cancer phototherapy. Biomaterials *276*, 121035. https://doi.org/10.1016/j.biomaterials.2021.121035.

86. Zhang, L., Tang, L., Jiang, Y., Wang, C., Huang, L., Ding, T., Zhang, T., Li, H., and Xie, L. (2023). GE11-antigen-loaded hepatitis B virus core antigen virus-like particles efficiently bind to TNBC tumor. Front. Oncol. *13*, 1110751. https://doi.org/10.3389/fonc.2023.1110751.

87. Mann, A., Shukla, V., Khanduri, R., Dabral, S., Singh, H., and Ganguli, M. (2014). Linear short histidine and cysteine modified arginine peptides constitute a potential class of DNA delivery agents. Mol. Pharm. *11*, 683–696. https://doi.org/10.1021/mp400353n.

88. Lo, S.L., and Wang, S. (2008). An endosomolytic Tat peptide produced by incorporation of histidine and cysteine residues as a nonviral vector for DNA transfection. Biomaterials *29*, 2408–2414. https://doi.org/10.1016/j.biomaterials.2008.01.031.

89. Huang, S., Zhu, Z., Jia, B., Zhang, W., and Song, J. (2021). Design of acid-activated cell-penetrating peptides with nuclear localization capacity for anticancer drug delivery. J. Pept. Sci. *27*, e3354. https://doi.org/10.1002/psc.3354.

90. Le Jeune, M., Secret, E., Trichet, M., Michel, A., Ravault, D., Illien, F., Siaugue, J.M., Sagan, S., Burlina, F., and Ménager, C. (2022). Conjugation of Oligo-His Peptides to Magnetic gamma-Fe(2)O(3)@SiO(2) Core-Shell Nanoparticles Promotes Their Access to the Cytosol. ACS Appl. Mater. Interfaces *14*, 15021–15034. https://doi.org/10.1021/acsami.2c01346.

91. Molino, N.M., Bilotkach, K., Fraser, D.A., Ren, D., and Wang, S.W. (2012). Complement activation and cell uptake responses toward polymer-functionalized protein nanocapsules. Biomacromolecules *13*, 974–981. https://doi.org/10.1021/bm300083e.

92. Xu, Q., Ensign, L.M., Boylan, N.J., Schön, A., Gong, X., Yang, J.C., Lamb, N.W., Cai, S., Yu, T., Freire, E., and Hanes, J. (2015). Impact of Surface Polyethylene Glycol (PEG) Density on Biodegradable Nanoparticle Transport in Mucus ex Vivo and Distribution in Vivo. ACS Nano *9*, 9217–9227. https://doi.org/10.1021/acsnano.5b03876.

93. Chen, X., Liu, Y., Wang, L., Liu, Y., Zhang, W., Fan, B., Ma, X., Yuan, Q., Ma, G., and Su, Z. (2014). Enhanced humoral and cell-mediated immune responses generated by cationic polymer-coated PLA microspheres with adsorbed HBsAg. Mol. Pharm. *11*, 1772–1784. https://doi.org/10.1021/mp400597z.

94. Xiao, K., Li, Y., Luo, J., Lee, J.S., Xiao, W., Gonik, A.M., Agarwal, R.G., and Lam, K.S. (2011). The effect of surface charge on in vivo biodistribution of PEG-oligocholic acid based micellar nanoparticles. Biomaterials *32*, 3435–3446. https://doi.org/10.1016/j.biomaterials.2011.01.021.

95. Calhoun, K.A., and Swartz, J.R. (2006). Total amino acid stabilization during cell-free protein synthesis reactions. J. Biotechnol. *123*, 193–203. https://doi.org/10.1016/j.jbiotec.2005.11.011.

96. Stark, J.C., Huang, A., Nguyen, P.Q., Dubner, R.S., Hsu, K.J., Ferrante, T.C., Anderson, M., Kanapskyte, A., Mucha, Q., Packett, J.S., et al. (2018). BioBits Bright: A fluorescent synthetic biology education kit. Sci. Adv. *4*, eaat5107. https://doi.org/10.1126/sciadv.aat5107.

97. Zawada, J., and Swartz, J. (2005). Maintaining rapid growth in moderate-density Escherichia coli fermentations. Biotechnol. Bioeng. *89*, 407–415. https://doi.org/10.1002/bit.20369.

STAR★METHODS

KEY RESOURCES TABLE

REAGENT or RESOURCE	SOURCE	IDENTIFIER
Antibodies		
Monoclonal Anti-Dengue Virus Type 2 Envelope Protein, Clone 3H5-1	BEI Resources (NIH)	NR-2556; RRID: AB930481
Bacterial and virus strains		
BL21(DE3) Competent E. coli	New England Biolabs (NEB)	C2527H
Escherichia coli strain KC6	Calhoun et al.[95]	N/A
NEB® 5-alpha Competent E. coli	New England Biolabs (NEB)	C2987H
Chemicals, peptides, and recombinant proteins		
Alexa Fluor™ 750 maleimide	Invitrogen	cat. # A30459
Alexa Fluor™ 568 maleimide	Invitrogen	cat. # A20341
Alexa Fluor™ 488 maleimide	Invitrogen	cat. # A10254
Mertansine	MedChemExpress	cat. # HY-19792
TCO-PEG4-DBCO	BroadPharm	cat. # BP-24160
sulfo TCO-maleimide	ClickChemistryTools	cat. # 1355
methyltetrazine-DBCO linker	ClickChemistryTools	cat. # 1022
sulfosuccinimidyl 4-(N-maleimidomethyl)cyclohexane-1-carboxylate	ThermoFisher	cat. # 22322
N-β-maleimidopropionic acid hydrazide	ThermoFisher	cat. # 22297
Experimental models: Organisms/strains		
Mouse: C57BL/6J	Jackson Laboratory	Strain #:000664
Mouse: J:NU	Jackson Laboratory	Strain #:007850
Oligonucleotides		
CpG DNA 5'{C2Ald.}{AmC6.}TCCATGACGTTCCTGACGTT3′	Trilink	N/A
Recombinant DNA		
pY71 Vector	Lu et al.[22]	N/A
pUC19 Vector	New England Biolabs (NEB)	N3041S
pJL1-sfGFP	Stark et al.[96]	Addgene Plasmid #102634
pJL1-DsbC	Jewett Lab	N/A
pUC19-DENV2	This Paper	N/A
pUC19-HBc	This Paper	N/A
Software and algorithms		
ImageJ	NIH	https://imagej.net/ij/

EXPERIMENTAL MODEL AND SUBJECT DETAILS

The mice were purchased from Jackson laboratory (Sacramento, CA). The C57BL/6J strain was used for the black domestic mice and the J:NU (007850) strain was used for the athymic nude mice. The mice were 6-8 weeks old. The mice were housed under standard conditions and the work was approved by the Stanford University Institutional Animal Care and Use Committee (IACUC).

METHOD DETAILS

Materials

Unless otherwise stated below, all chemicals were purchased from Fisher Scientific (Waltham, MA).

Cloning

The expression cassette from the pY71 vector[22] was cloned into the pUC19 backbone (New England Biolabs, Ipswich (MA), cat.# N3041S). The HBc 1-149 and domain 3 of the dengue envelop protein serotype 2 genes were inserted into this modified vector via Gibson assembly after PCR extension to provide base homology overlaps. The genes underwent codon optimization for

E. coli. pJL1_sfGFP[96] was kindly donated by the Jewett Lab. Point mutations and extensions were performed via quick change using the Q5 polymerase from New England Biolabs (Ipswich (MA), cat.# M0491). All plasmids were prepared following the Qiagen Maxiprep protocol and eluted with sterile water (Qiagen, Germantown (MC), cat.# 12162). All plasmids were sequenced to confirm accuracy. NEB® 5-alpha Competent E. coli (NEB, cat.# C2987H) were used for all plasmid preparations. Amino acid sequences are provided in Data S1.

Cell-free protein synthesis (CFPS)

All CFPS reactions were conducted using a modified version of the PANOxSP protocol.[42] For the HBc protein KC6 extract[95] was used, which was prepared using defined media[97] and a cell resuspension buffer containing 60 mM potassium glutamate, 14 mM magnesium glutamate and 40 mM HEPES pH 7.2. For global methionine replacement in HBc, methionine was substituted with 6 mM AHA (Iris Biotech, Marktredwitz (Germany), cat.# HAA5730). The HBc reactions were incubated for 20-24 hours at room temperature or overnight at 30°C. For the DENV2 envelope domain 3 (ED3) and sfGFP-IGIGIG CFPS, BL21 extract was prepared using 2x YTPG media and BL21(DE3) Competent E. coli (NEB, cat.# C2527H). The cells were washed three times and resuspended in 60 mM potassium glutamate, 14 mM magnesium glutamate and 50 mM HEPES pH 7.2. For DENV2 ED3, the extract was treated prior to use with 0.5 mM iodoacetamide for 30 minutes at room temperature to facilitate disulfide bond formation and stabilization.[43] The reaction was protected from light. To promote correct disulfide bond formation, 4 mM oxidized and 1 mM reduced glutathione were added. The final potassium glutamate concentration of the reaction was 50 mM, 0.01% Brij 58 was added for increased protein solubility, and 10 μM DsbC was added to facilitate correct disulfide bond formation. The DENV2 reactions were conducted at 30°C overnight. For sfGFP-IGIGIG, total potassium glutamate concentration was 175 mM and the reaction were conducted at 30°C overnight. CFPS reactions were performed at scales ranging in total from 100 μl to 30 mL with separation into 25 μl or ca. 10 mL reactions (depending on the size of the reaction) conducted in 2 ml Eppendorf tubes or 10 cm diameter petri dishes, respectively.

Using C^{14} to assess CFPS yields

To measure total as well as soluble protein yields, small scale CFPS reactions were performed with 2 μM ^{14}C-leucine (L-[^{14}C (U)]), (PerkinElmer, Waltham (MA), cat.# NEC279E250UC) additional to 2 mM unlabeled leucine. Incorporated ^{14}C-leucine was measured by spotting 5 μl of sample on Whatman filter paper and washing 3 times with 5% trichloroacetic acid for 15 minutes each at 4°C to precipitate the proteins and remove unincorporated ^{14}C-leucine. For soluble protein measurements, samples were centrifuged for 15 minutes at 10,000 g prior to spotting the supernatant; and, for total radioactivity measurements, samples were spotted as described above, but not washed. Radioactivity was measured using a Beckman LS6000 liquid scintillation counter.

SDS-PAGE and autoradiogram

Sodium dodecyl sulfate–polyacrylamide gel electrophoresis (SDS-PAGE) used NuPAGE™ 4 -12% Bis-Tris Gels (Invitrogen, Waltham (MA), cat.# NPO323BOX) in MES buffer. SeeBlue™ Plus2 Prestained Standard (Invitrogen, Waltham (MA), cat.# LC5925) was used for autoradiograms, while Mark12™ Unstained Standard (Invitrogen, Waltham (MA), cat.# LC5677) was used for all other gels. Electrophoresis was conducted for 30 minutes at 200 V in MES buffer. Autoradiograms were imaged using a Typhoon FLA 9500 (GE Healthcare) instrument. For non-radioactive gels, proteins were visualized using SimplyBlue™ Safe Stain (Novex, Wadsworth (OH), cat.#: LC6065). Proteins were either in reduced (DTT) or non-reduced form as indicated in the figure legends.

Nickel nitriloacetic acid (Ni-NTA) purification

Ni-NTA was used to purify the HBc monomers via their C-terminal 6xHis-tag. The Ni-NTA column was equilibrated with 5 column volumes (CVs) of 50 mM NaCl, 10 mM Tris-HCl pH 8, 1.5 M Urea, 0.02% polysorbate 20 (Tween 20). The sample was buffer exchanged into the loading buffer using PD-10 desalting columns packed with Sephadex G-25 resin following manufacturer's instructions (Cytiva, Marlborough (MA), cat.# 17085101). The same was done for all other buffer exchanges. After loading the sample and an approximately 30 minutes incubation period, the column was initially washed with ca. 2 CVs of 50 mM NaCl, 10 mM Tris-HCl pH 8, 20 mM imidazole, 5 mM DTT over 10-15 minutes to reduce any disulfide bonds in HBc dimers. Finally, 3-5 CVs of 50 mM NaCl, 10 mM Tris-HCl pH 8 and 20 mM imidazole were applied to remove the DTT. Elution was effected by a 50 mM NaCl, 10 mM Tris-HCl pH 8 and 450 mM imidazole solution and appropriate fractions were collected. Protein concentrations were measured using the NanoOrange® Protein Quantitation Kit (Invitrogen, Waltham (MA), cat.# N6666) and a SpectraMax iD3 (Molecular Devices) plate reader. The entire purification process was performed under anaerobic conditions in an N_2 only (dry) glove box.

For DENV2, the Ni-NTA column was equilibrated with 50 mM Tris-HCl pH 8, 100 mM NaCl and 0.02% Tween 20. The sample was buffer exchanged into the equilibration buffer and incubated for ca. 30 minutes on the column. Next, the column was washed with 50 mM Tris-HCl pH 8, 100 mM NaCl, 0.02% Tween 20 and 25 mM imidazole. DENV2 was eluted with 50 mM Tris-HCl pH 8, 100 mM NaCl, 0.02% Tween 20 and 300 mM imidazole. Elution fractions with the product were buffer exchanged into 1x phosphate buffered saline (PBS), pH 7.0 and 0.02% Tween 20. The entire purification was performed under anaerobic conditions to prevent dimer formation.

Strep-Tactin XT Sepharose affinity purification of sfGFP-IGIGIG

After overnight incubation, the CFPS reaction was centrifuged at 10,000xg for 5 minutes to pellet any insoluble components. The supernatant was buffer exchanged into the equilibration buffer 100 mM Tris-HCl, 150 mM NaCl, 1 mM EDTA, pH 8.0 using PD-10

columns. The buffer exchanged sample was then loaded onto an equilibrated Strep-Tactin XT Sepharose column (Cytiva, Marlborough (MA), cat.# 29401324). After 10 CV of washes with the equilibration buffer, the sfGFP-IGIGIG was eluted using 100 mM Tris-HCl, 150 mM NaCl, 1 mM EDTA, 50 mM biotin, pH 8.0. The eluted protein was then buffer exchanged into 1x PBS pH 7.4, 15% (w/v) sucrose, flash frozen using liquid nitrogen and stored at -80°C.

DsbC expression and purification protocol

The pJL1-DsbC plasmid was kindly provided to us by the Jewett lab. The DsbC was modified to have an N-terminal Strep-2 tag and transformed into BL21(DE3) competent E. coli (NEB, cat.# C2527H). The cells were grown for 8 hours in two 5 mL LB media culture supplemented with kanamycin at 37°C and 250 rpm. Two 100 ml cultures of 2xYTP, pH7.3 were inoculated with the 5 ml cultures and grown overnight at 37°C and 250 rpm. The next day, 8 L of 2x YTP, pH 7.3 were inoculated to a starting OD_{600} of 0.2. Once the OD_{600} reached 0.6, 0.5 mM IPTG was added. After reaching an OD_{600} of 4-5, the cells were harvested by centrifugation at 4000 g for 20 minutes at 10°C. The cells were washed in 5 ml per gram of wet cells using 100 mM Tris-HCl, 150 mM NaCl, 1 mM EDTA, pH 8.0 (binding buffer) and centrifuged at 10,000 g, 10 °C for 15 minutes. The pellets were stored at -80°C until the next day. The pellets were then resuspended in 1-2 ml of binding buffer. Once fully resuspended, 1 μL of benzonase nuclease (Millipore Sigma, Milwaukee (WI) cat.# E1014) per 10 mL of resuspension and 1 ml of Halt™ Protease and Phosphatase Inhibitor Cocktail (100X) (ThermoFisher Scientific, Waltham (MA), cat.# 78440) per 100 ml of resuspended cells was added. Once mixed, the cells were lysed by passing through a C-50 Avestin Homogenizer three times at pressures between 18,000-23,000 psi. The lysed cells were rotated at 4° C for fifteen minutes to allow the benzonase to degrade genomic DNA. The cell debris was then pelleted by centrifugation at 12,000 g for 10 minutes. The supernatant was then centrifuged once again for 15 minutes. After equilibration of the StrepTactin XT resin (Cytiva, Marlborough (MA), cat.# 29401322) with the binding buffer, 2 ml of sample per ml of resin were loaded onto the column. The column was washed with 12 CV of binding buffer and eluted with 8 CV of 100 mM Tris-HCl, 150 mM NaCl, 1 mM EDTA, 50 mM biotin, pH 8.0 (elution buffer). Fractions containing DsbC were then buffer exchanged into 1x PBS, pH 7.40 and sucrose was added (10% w/v) before flash freezing the protein samples and storing them at -80°C.

VLP assembly and stabilization

Before assembly, the HBc monomers were buffer exchanged into 10 mM Tris-HCl pH 7.4, 50 mM NaCl and 0.05% Tween 20 to remove the imidazole. DMSO was then added to a concentration of 2%. One-step assembly was conducted by adding NaCl to 1 M over 5 minutes followed by overnight incubation. For the two-step assembly procedure, NaCl was increased to 100 - 300 mM over 2 minutes followed by a 5 to 10 minute incubation. NaCl was then increased to 1 M over 5 minutes and the final solution incubated overnight or for a minimum of 2 hours. All NaCl additions were conducted with vigorous mixing on a stir plate. Both assembly processes were performed under anaerobic conditions (at room temperature) to prevent premature intradimer disulfide bond formation. The assembled VLPs were finally stabilized by forming intra- and interdimer disulfide bonds by adding 500 μM hydrogen peroxide and incubating for at least 30 minutes.

Loading

AlexaFluor and mertansine

VLPs were loaded with Alexa Fluor™ 750 maleimide (AF750M, Invitrogen, Waltham (MA), cat. #A30459) using a 0.22 to 1 molar ratio of added dye to total HBc monomer. For the one-step assembly procedure, AF750M dye was added immediately after the NaCl addition. For the two-step assembly method, the dye was added after the initial 10-minute incubation step at low NaCl concentration. For Alexa Fluor™ 488 and 568 maleimide (AF488M, Invitrogen, Waltham (MA), cat.# A10254 and A20341) loading, the same procedure was used with the exception of a 0.5 to 1 molar ratio and 0.35 to 1 molar ratio of dye to total HBc monomer respectively. For the simultaneous loading of mertansine (MedChemExpress, Monmouth Junction (NJ), cat. #HY-19792) and AF750M, the dye was added 8 minutes after addition of 300 mM NaCl. After an additional 2-minute incubation at 300 mM NaCl, mertansine was added at a 2.5 molar ratio of mertansine to monomer. After a further 5-minute incubation at the low NaCl concentration, the 5-minute increase to 1 M NaCl was initiated. Prior to loading, mertansine was incubated with 10 mM DTT for 10 minutes and then precipitated by increasing the NaCl concentration to 3 M. The reduced mertansine was washed twice with 3 M NaCl and resuspended in 100% DMSO to reach a final concentration of 3 - 5 mM. The assembly reaction was incubated for a minimum of 2 hours. AlexaFluor loading was analysed by measuring the amount of fluorescence after VLP disassembly and comparing it to the number of VLPs present. Mertansine loading was quantified via HPLC.

CpG DNA

For CpG DNA loading, CpG DNA (Trilink, San Diego (CA), custom made with a 5′aldehyde) was incubated with the BMPH linker (N-β-maleimidopropionic acid hydrazide) (ThermoFisher, Waltham (MA), cat.# 22297) in a 1:0.75 molar ratio in 1x PBS pH 7.0 at room temperature for 4 hours. For loading the following two-step assembly procedure was used: after an initial DMSO addition to 2%, NaCl was added over 2 minutes to a concentration of 300 mM. Following a 5-minute incubation period, the cargo was added followed by another incubation of 2 minutes. The remaining NaCl was added over 5 minutes to reach a 1 M final concentration. The assembly reaction was incubated for a minimum of 2 hours. CpG DNA loading was analysed via SDS-PAGE and subsequent densitometry analysis using ImageJ. Nucleotide sequence is provided in Data S2.

sfGFP-IGIGIG

sfGFP-IGIGIG loading was performed using an NHS-ester maleimide linker, sulfosuccinimidyl 4-(N-maleimidomethyl) cyclohexane-1-carboxylate (ThermoFisher, Waltham (MA) cat.# 22322). First, the linker was incubated with the protein at 4°C overnight at a 3 to 1 ratio of linker to protein. Loading was performed using the following modified two-step assembly: after an initial DMSO addition to 2%, NaCl was added to a concentration of 100 mM. Following a 10-minute incubation period, the 26.5 sfGFP per VLP (monomer concentration divided by 240) were added followed by another 10-minute incubation. The remaining NaCl was added over 5 minutes to achieve a 1 M final concentration. The assembly reaction was incubated for a minimum of 2 hours. Loading of sfGFP was confirmed by fluorescence measurement after SEC and concentration with a 100 kD cut-off membrane.

Size-exclusion chromatography (SEC)

The fully assembled VLPs were isolated from the partially assembled multimers, unassembled monomers, excess cargo molecules, and aggregates using SEC with Sephacryl S-500 high resolution resin (Cytiva, Marlborough (MA), cat.# 17061301). The column was first equilibrated with 5 CV of PBS pH 7.4 with 0.01% Tween 20 (Figures S2A and S2B). Before loading, the sample was concentrated to ca. 5% of the CV and fractions of approximately 5% the CV were collected.

Calculation of assembly efficiency

Assembly efficiency was calculated using the 280 nm absorbance of the SEC column fractions after using DLS analysis to identify fractions with only assembled VLPs.

VLP disassembly

To disassemble VLPs for analysis of loading, VLPs were incubated in 0.2% SDS and 100 mM DTT for 5 to 30 minutes at room temperature followed by a 10 minute incubation at 50°C. Disassembly also enabled analysis of fluorophore self-quenching.

To disassemble VLPs for analysis of conjugation efficiency by SDS-PAGE, 80 mM DTT together with the SDS sample buffer were added to the sample and incubated at 94°C for 10 minutes.

Click conjugation

Copper-catalyzed azide–alkyne cycloaddition (CuAAC)

CuAAC were performed using 2 mM Tetrakis(acetonitrile)copper(I) hexafluorophosphate and 6 mM BTTAA (ClickChemistryTools, Scottsdale (AZ), cat.# 1237) in 25 mM phosphate buffer pH 8. HBc monomer concentration was 15 μM and mPEG 5000 alkyne was added in a 1 to 10x molar ratio. The reactions were conducted in an anaerobic glove box.

Strain-promoted azide–alkyne cycloaddition (SPAAC)

To conjugate methoxypolyethylene glycol thiol (Sigma-Aldrich, St. Loius (MO), cat.# 729159) to the VLP, mPEG thiol was first incubated with a DBCOM linker (Click Chemistry Tools, Scottsdale (AZ), cat.# 1230) in a 1:1.5 molar ratio in PBS pH 7.0 for 1 hour. The unreacted linker was removed by SEC using Sephadex G-25 resin (Cytiva, Marlborough (MA), cat.# 17085101). Absorbance of the collected fractions was measured at 309 nm. The conjugated mPEG thiol DBCOM linker was then incubated in a 5:1 to 10:1 molar ratio of mPEG thiol DBCOM linker to HBc monomers overnight at room temperature. Conjugation was confirmed with SDS-PAGE. Unreacted ligands were removed by SEC using 1x PBS pH 7.4 0.02% Tween 20.

For conjugation of the DBCOM linker to DENV2, the linker was incubated with the protein in a 5 to 1 ratio, respectively, for 4 hours in 1x PBS buffer pH 7.0 with 0.02% Tween 20. The linker was removed by Sephadex G-25 SEC, and linker attachment was confirmed by measuring free sulfhydryl using the Thiol Fluorescent Detection Kit (Invitrogen, Waltham (MA), cat.# EIARSHF). For attachment to the VLP, the linker modified DENV2 protein was incubated overnight with the VLP in a 1 to 3.5 molar ratio of HBc monomer to DENV2 protein. Conjugation was confirmed by SDS-PAGE.

Inverse electron demand Diels–Alder cycloaddition (IEDDA)

For conjugation using IEDDA mechanism, the trans-cyclooctene (TCO) PEG4 DBCO (BroadPharm, San Diego (CA), cat. # BP-24160) and sulfo TCO-maleimide (ClickChemistryTools, Scottsdale (AZ), cat. # 1355) linkers were incubated in a 10:1 ratio of linker to mPEG 5000 azide (BroadPharm, San Diego (CA), cat. # BP-23444) and DENV2 respectively. The HBc VLPs were incubated with a 10x molar ratio of the methyltetrazine-DBCO linker (ClickChemistryTools, Scottsdale (AZ), cat. # 1022). The linker conjugations were performed in 1x PBS pH 7.2, 0.02% Tween 20, 10% DSMO at room temperature overnight, the maleimide reaction was performed in an anaerobic glove box. After linker conjugation the unreacted linkers were removed via Sephadex G-25 SEC. The IEDDA conjugation was performed in ratios of ligand to HBc monomer of 0.25 - 1.5 to 1. The HBc monomers concentration was 15 μM. The reactions were performed at room temperature for 4 to 16 hours in 1x PBS pH 7.2, 0.02% Tween 20, 10% DSMO.

High performance liquid chromatography (HPLC)

Mertansine loading was verified using reverse-phase HPLC using an Agilent 1260 Infinity II instrument. 25 μL of disassembled VLPs were injected onto a POROSHELL 300SB-C8 column (Agilent, Santa Clara (CA), cat.# 660750-906) and mertansine was analyzed at 252 nm. Mobile phase A consisted of 10 mM ammonium acetate (pH 7.0) and mobile phase B was 100% acetonitrile. The mobile phase pump rate was 0.2 ml/min. After sample injection, an initial gradient of 25% B to 50% B over 26 minutes was followed by a

50% B to 100% B gradient for a further 4 minutes. The solvent composition was then held at 100% B for 17.5 min and finally returned to 25% B over 1.75 min. The column was then equilibrated for 35 min prior to the next injection. All operations were conducted at room temperature.

DLS

DLS analysis was performed using the Malvern Zetasizer Nano ZS. 40 μl of sample were placed into each Malvern Panalytical 40 μl cuvette (Malvern Panalytical, Westborough (MA), cat.# ZEN0040). For the material (VLPs) the refractory index was set to 1.45, absorption to 0.001. For the dispersant, temperature was set to 23°C, viscosity to 0.9308 cP, and the refractory index to 1.330. The sample was allowed to equilibrate for 30 seconds. 3 measurements were obtained for each sample, each containing 9 runs of 10 seconds duration.

TEM

For TEM imaging, a 25 μM VLP sample (T=4) was prepared in 1x PBS buffer, pH 7.20. 5 μL of the sample was added to a plasma-treated copper/formvar grid (Ted Pella, Redding (CA), cat. # 01813-F). After three minutes, the corner of a triangular paper (G-Bio-Sciences cat. # BTNM-0035) was moved around the edge of the grid to remove excess solution. The applied sample was left to dry for twenty-four hours at room temperature. Next, 5 μL of 1% uranyl acetate (Electron Microscopy Sciences, Hatfield (PA), cat. # 22400-2) was added to the loaded grids. After three minutes, excess liquid was removed as before. The washed grid was finally dried for twenty-four hours. The entire procedure was carried out in an anaerobic glove box. Samples were analyzed using a FEI Titan TEM (Hilsboro, OR), at 80 kV.

Immunoprecipitation of HBc VLP conjugated with DENV2

Recombinant Protein G - Sepharose™ 4B beads (ThermoFisher, Waltham (MA) cat.# 101242) were washed three times with 10 ml of 1x PBS pH 7.4, 0.02% Tween 20. Centrifugation was performed at 400 g for 3 minutes at 4°C. 1 μg of monoclonal DENV2 clone 3H5-1 antibodies were added per 10 μl of beads. The antibodies were obtained through BEI Resources (BEI resources, Manassas (VA)), NIAID, NIH: Monoclonal Anti-Dengue Virus Type 2 Envelope Protein, Clone 3H5-1 (produced *in vitro*), NR-2556. The antibodies were incubated with the beads at 4°C while rotating for 2 hours. The beads were washed as before to remove all unbound antibodies. 40 μl of 45 to 90 μg/ml of HBc VLPs with and without DENV2 conjugated and AF750 loaded were added to 15 μl of 50/50% suspension of antibody coated beads in 1x PBS pH 7.4 0.02% Tween 20 buffer. After 45 minutes incubation at room temperature while rotating and 10 minutes centrifugation at 400 g at 4°C the fluorescence of the supernatant was measured.

VLP sample freezing

The assembled VLPs were flash frozen using liquid nitrogen and stored in 10% trehalose, 1x PBS pH 7.4, 0.02% Tween 20 at – 80°C.

ImageJ

The software ImageJ was used for densitometry analysis of stained SDS-PAGE gels.

Figures

Graphical figures were created using BioRender.com.

QUANTIFICATION AND STATISTICAL ANALYSIS

All values are reported as mean plus standard deviation of the mean and significance was calculated using a two-tailed t-test. Microsoft excel was used for all calculations. P-values ≤ 0.05 were considered significant.